The Meteoritical Society

Meteoritics & Planetary Science 51, Nr 12, 2293–2315 (2016)
doi: 10.1111/maps.12726

Mineral chemistry of the Tissint meteorite: Indications of two-stage crystallization in a closed system

Yang LIU[1,2*], Ioannis P. BAZIOTIS[2,3], Paul D. ASIMOW[4], Robert J. BODNAR[5], and Lawrence A. TAYLOR[2]

[1]Jet Propulsion Laboratory, California Institute of Technology, Pasadena, California 91109, USA
[2]Planetary Geosciences Institute, Department of Earth and Planetary Sciences, University of Tennessee, Knoxville, Tennessee 37996, USA
[3]Department of Natural Resources Management and Agricultural Engineering, Laboratory of Mineralogy and Geology, Agricultural University of Athens, 11855 Athens, Greece
[4]Division of Geological and Planetary Sciences, California Institute of Technology, Pasadena, California 91125, USA
[5]Department of Geosciences, Virginia Tech, Blacksburg, Virginia 24061, USA
[*]Corresponding author. E-mail: yang.liu@jpl.nasa.gov

(Received 04 February 2016; revision accepted 10 July 2016)

Abstract–The Tissint meteorite is a geochemically depleted, olivine-phyric shergottite. Olivine megacrysts contain 300–600 μm cores with uniform Mg# (~80 ± 1) followed by concentric zones of Fe-enrichment toward the rims. We applied a number of tests to distinguish the relationship of these megacrysts to the host rock. Major and trace element compositions of the Mg-rich core in olivine are in equilibrium with the bulk rock, within uncertainty, and rare earth element abundances of melt inclusions in Mg-rich olivines reported in the literature are similar to those of the bulk rock. Moreover, the P Kα intensity maps of two large olivine grains show no resorption between the uniform core and the rim. Taken together, these lines of evidence suggest the olivine megacrysts are phenocrysts. Among depleted olivine-phyric shergottites, Tissint is the first one that acts mostly as a closed system with olivine megacrysts being the phenocrysts. The texture and mineral chemistry of Tissint indicate a crystallization sequence of: olivine (Mg# 80 ± 1) → olivine (Mg# 76) + chromite → olivine (Mg# 74) + Ti-chromite → olivine (Mg# 74–63) + pyroxene (Mg# 76–65) + Cr-ulvöspinel → olivine (Mg# 63–35) + pyroxene (Mg# 65–60) + plagioclase, followed by late-stage ilmenite and phosphate. The crystallization of the Tissint meteorite likely occurred in two stages: uniform olivine cores likely crystallized under equilibrium conditions; and a fractional crystallization sequence that formed the rest of the rock. The two-stage crystallization without crystal settling is simulated using MELTS and the Tissint bulk composition, and can broadly reproduce the crystallization sequence and mineral chemistry measured in the Tissint samples. The transition between equilibrium and fractional crystallization is associated with a dramatic increase in cooling rate and might have been driven by an acceleration in the ascent rate or by encounter with a steep thermal gradient in the Martian crust.

INTRODUCTION

The shergottite groups constitute the majority (~83%) of known Martian meteorites, even though they represent only a minute fraction of all meteorites discovered to date (~0.26%, according to the Meteoritical Bulletin Database). These mafic to ultramafic rocks provide samples that can be used to decipher and understand the magmatic differentiation and evolution of Mars. Occasionally, the fiery delivery of these samples to Earth is observed, and the rapidly recovered meteorites represent the least terrestrially

weathered Martian samples, making them critical for studying a diverse range of processes that occurred on Mars. The Tissint meteorite is one such sample. On July 18, 2011, a fireball was witnessed in the region of the Oued Draa Valley, east of Tata, Morocco. Within a few months, pieces of this fall were recovered in the area between Tata and the village of Tissint, and the meteorite was named Tissint. In contrast to previous fall samples (Shergotty, Zagami, Nakhla, and Chassigny), Tissint is the first fall of olivine-phyric lithology, representing a unique opportunity to examine minerals that are least affected by terrestrial weathering.

The total mass of the Tissint meteorite recovered to date is ~7 kg (http://www..lpi.usra.edu/meteor/index.php?code = 54823). For a meteorite of this size, some petrologic diversity is to be expected. The initial description and confirmation of the Martian origin was made by Irving et al. (2012), and the initial comprehensive description was reported by Chennaoui Aoudjehane et al. (2012). A detailed petrologic study by Balta et al. (2015) further investigated the crystal-size distribution of olivine and rare earth element variations in minerals. These studies observed that Tissint is unique in that it is depleted in highly incompatible elements (e.g., Rb, La, Ce), but is enriched in moderately incompatible elements compared to the other depleted shergottites. The Tissint meteorite is also one of the most intensely shocked Martian meteorites, containing spinel-structured olivines (ahrensite and ringwoodite), jadeite-group pyroxene (tissintite), $CaTi_2O_4$-structured (CT) chromite, and possibly diamond (Baziotis et al. 2013; El Goresy et al. 2013; Hu et al. 2013; Kuchka et al. 2013; Summerson et al. 2013; Ma et al. 2014, 2015, 2016; Walton et al. 2014). Among these findings, ahrensite and tissintite are the first new minerals identified in Martian rocks (Ma et al. 2014). Baziotis et al. (2013) estimated that the Tissint meteorite was derived from a large impactor and crater on Mars based on the assumption of diffusive crystallization of 1 μm ringwoodite grains. However, additional investigation by Walton et al. (2014) and Ma et al. (2016) demonstrated that ringwoodite is actually composed of 0.05–0.4 μm grains. Additionally, the aggregation and preservation of original zoning in ringwoodite suggest that solid-state transformation is likely the main mechanism for ringwoodite formation in Tissint (Walton et al. 2014; Ma et al. 2016). Such a process is rapid and would occur on a time scale of tens of nano-seconds (Tschauner et al. 2009). Thus, the use of grain size and the diffusive model (Baziotis et al. 2013) significantly overestimated the minimum duration of the shock process. Nonetheless, the reports of multiple high-pressure phases in the Tissint meteorite by several research groups show that this is one of the best samples for examining shock metamorphism in Martian rocks. In addition, the Tissint meteorite contains abundant large and glassy impact pockets, which provide excellent materials for investigating water and other volatiles in this basaltic meteorite (Chen et al. 2015).

In spite of the shock features, the Sm-Nd isotopic system of the Tissint meteorite yields a reasonable isochron age, reported to be from 472 ± 36 Ma to 616 ± 67 Ma according to different research groups, whereas the Rb-Sr isotopic system appears to be disturbed by shock (Grosshans et al. 2013; Park et al. 2013; Brennecka et al. 2014; Shih et al. 2014). The Lu-Hf isotopic system suggests an age of 583 ± 86 Ma for Tissint, overlapping with the age (~574 Ma) of Dhofar (Dho) 019 within uncertainties (Grosshans et al. 2013). Crystallization ages and the rare earth element (REE) pattern of the Tissint meteorite are consistent with this meteorite being a member of the group of shergottites that display a strong depletion in highly incompatible elements (Chennaoui Aoudjehane et al. 2012; Balta et al. 2015). These shergottites also show low initial $^{87}Sr/^{86}Sr$, high initial $^{143}Nd/^{142}Nd$, and $^{176}Hf/^{177}Hf$ values that are consistent with a mantle source that was already depleted in these incompatible elements well before the igneous event dated by the isochrons (e.g., Borg et al. 2002, 2003; Borg and Draper 2003; Symes et al. 2008; Shih et al. 2014). Other well-studied members of this group include olivine-phyric shergottites Yamato (Y)-980459, Dho 019, Dar al Gani (DaG) 476, Sayh al Uhaymir (SaU) 005, Northwestern Africa (NWA) 1195, and aphyric shergottite Queen Alexandra Range (QUE) 94201. Concentrations of rare earth elements in the Tissint meteorite are higher than most shergottites in the depleted group, except for QUE 94201 (e.g., Chennaoui Aoudjehane et al. 2012; Balta et al. 2015). Here, we report characterization of mineralogy and geochemistry of our Tissint samples, with emphasis on features that are not reported in Chennaoui Aoudjehane et al. (2012) and Balta et al. (2015). In addition, in contrast to the suggestion of Balta et al. (2015) that olivine cores are antecrysts, we evaluate an alternative petrogenesis model in which the whole-rock of Tissint represents a liquid composition, from which the olivine megacrysts initially crystallized in equilibrium with the melt, followed by progressive fractional crystallization.

MATERIALS AND METHODS

A 10 g piece of the Tissint meteorite and three loose chips were obtained and used for this study. All of these chips were covered by fusion crust. Three thin sections from the 10 g piece (UT1 to UT3) and three

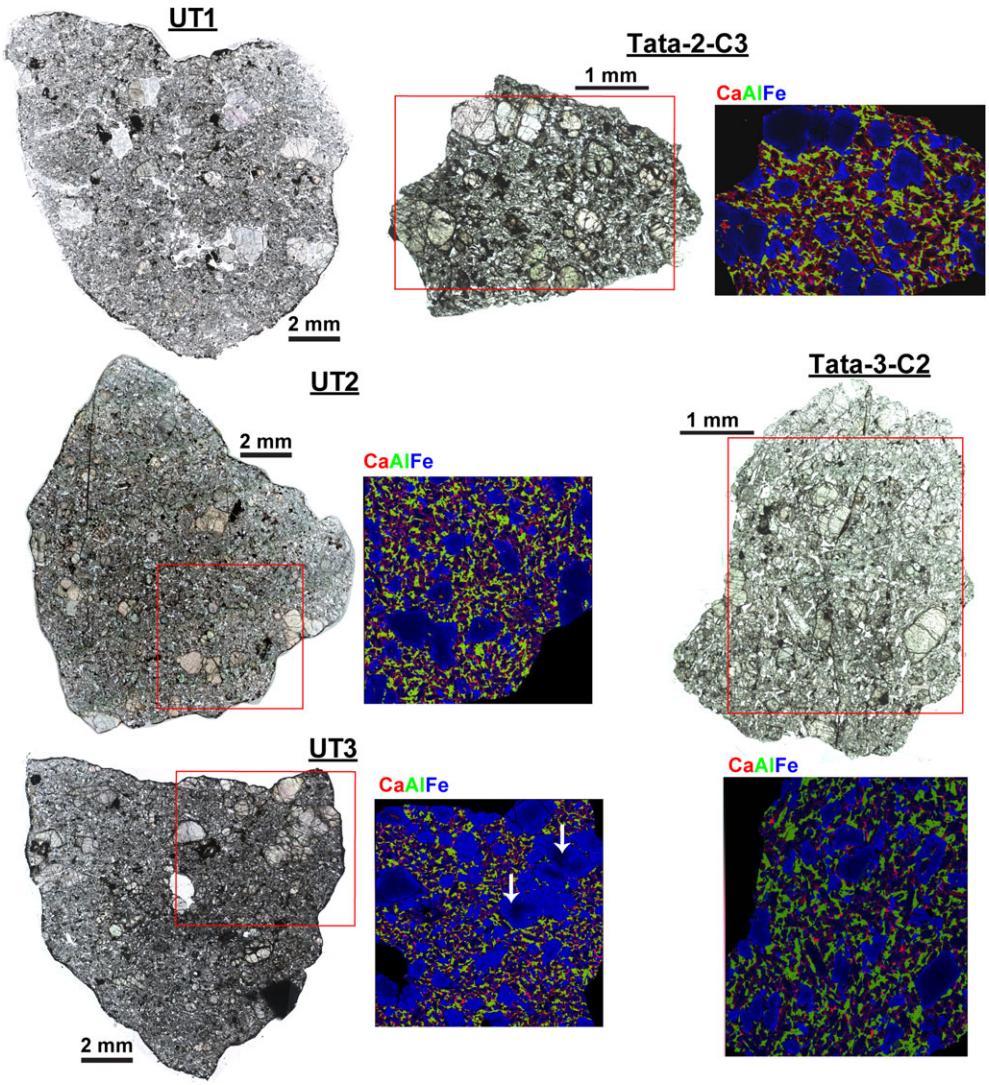

Fig. 1. Transmitted light images and false-colored Ca, Al, and Fe Kα maps (four of the five) of polished sections of the Tissint meteorite used in this study. Red rectangles mark the X-ray map locations. White arrows mark possible irregular cores. Refer to color figures in the online version.

thin sections from three loose pieces (Tata-1-C1 to C3, Tata-2-C1 to C3, and Tata-3-C1 to C3, Fig. 1) are the source of most data reported in this study. A seventh section, Tissint-B, was used for additional trace element analysis. Baziotis et al. (2013) reported high-pressure minerals in UT1 to UT3 (formerly referred to as MT-1, MT-2, MT-3). The petrography of these sections was examined using a petrographic microscope and a scanning electron microscope. Backscattered electron (BSE) images and elemental X-ray maps (Ca *K*α, Al *K*α, Fe *K*α, and Mg *K*α) of four sections were obtained using a Cameca SX100 electron microprobe (EMP) at the University of Tennessee with 15 keV accelerating potential and a 20 nA focused beam at a step size of 8–12 μm.

Mineral modes in Tissint were estimated from elemental maps. These images were imported into the image-processing software ImageJ, where the brightness levels of these maps (0-255) were converted to a histogram, displaying unique peaks corresponding to specific minerals. Therefore, by selecting threshold values separating a given peak from background and other peaks, the number of pixels for that specific mineral was counted in the corresponding X-ray maps. The number of pixels attributed to each mineral was divided by the total number of pixels in the whole section to obtain modal-area fraction of each mineral, which was taken to represent a volume fraction, given the absence of any obvious anisotropy in the mineral fabric. Errors associated with the measurement of the

modal abundances are a function of image resolution and the selection of the threshold values. Often, one mineral was estimated using multiple X-ray maps. Olivine can be distinguished from pyroxenes and plagioclase based on the lack of Al and Ca and higher Fe and Mg counts. Plagioclase displays no Mg and low Fe and is high in Al. Low-Ca pyroxene (Wo < 5) is distinguished from other phases by low Ca counts together with intermediate Fe and Mg counts. Sulfides contain the highest Fe counts, whereas phosphates display the highest Ca counts. Chromite can be discerned based on its moderate Al counts, but ulvöspinel and ilmenite require a Ti map. Therefore, Fe-Ti-Cr oxides were grouped together as one phase. Melt pockets were manually outlined for the modal estimate.

Quantitative major and minor element compositions of minerals and glasses were obtained with the Cameca SX100 EMP at the University of Tennessee and a JEOL JXA-8200 EMP at Caltech. Analytical conditions for olivine, pyroxene, and Fe-Ti-Cr oxides were 15 kV accelerating voltage, 20 nA beam current, and 1–2 μm beam diameter. Maskelynite, phosphate, sulfide, and glass were analyzed using a defocused beam of 5–10 μm size, an accelerating voltage of 15 kV, with a 10 nA beam current. Detection limits are typically <0.03 wt% for SiO_2, TiO_2, Al_2O_3, MgO, and CaO; <0.05–0.1 wt% for FeO, MnO, Cr_2O_3, NiO, Na_2O, K_2O, and P_2O_5. The Fe *K*α, P *K*α, Al *K*α, Ca *K*α, and Cr *K*α maps of two olivine megacrysts were collected using the EMP, with a focused beam of 15 kV voltage and 200 nA current, a step size of 2 μm, and a dwell time of ~0.5 s at each step.

Major, minor, and trace element compositions of selected phases were obtained using an Agilent 7500ce inductively coupled plasma–mass spectrometer (ICP-MS), coupled with a GeoLasPro 193 nm Excimer laser-ablation (LA) system, at the Department of Geosciences, Virginia Tech. The analytical procedure is broadly similar to that of Udry et al. (2012) and Pernet-Fisher et al. (2014). A NIST 610 glass standard was analyzed before and after every session. The background was counted for 50 sec before each LA-ICP-MS analysis. Laser conditions were a 5 Hz repetition rate, a 150 mJ output energy, and a fluence rate of 7–10 J/m^2 on the sample. We used different beam sizes for different minerals. The smaller spot (~24 μm) size was used for phosphate analysis, 24 and 32 μm diameter were commonly used for silicates and glass, and a few analyses were conducted on olivines using a 90 μm beam to evaluate whether the low signals of REEs are a result of insufficient sampling. Raw data for each time-resolved signal were processed offline using the stand-alone AMS ver. 1.0 analytical software (Mutchler et al. 2008). The time-lapse plots of each spot were examined, and only the plateau region was used to quantify the trace element abundances. For silicates and oxides, trace element abundances were calculated by normalization to 100 wt% oxide total. For spots with electron-probe data, the normalization method generally agrees within <10% with the method using EMP CaO or MgO values as internal standards. For phosphate, we calculated the trace element abundances by normalizing the LA-ICP-MS ^{40}Ca counts to CaO concentrations from the EMP analysis.

RESULTS

Petrography and Mineral Compositions

All sections of the Tissint meteorite display porphyritic textures, as reported previously (Fig. 1; Chennaoui Aoudjehane et al. 2012; Baziotis et al. 2013; Balta et al. 2015). Olivines occur as individual megacrysts or in clusters in our samples, as was also reported by Balta et al. (2015) (Fig. 2). In decreasing modal abundance, the Tissint meteorite contains pyroxenes (51–60 vol%), olivine (22–26 vol%), maskelynite (former plagioclase, 14–17 vol%), and minor phases (<10 vol%), including chromite–ulvöspinel solid-solution spinels, ilmenite, phosphates, sulfides, and impact-produced melts, similar to other Tissint chips (Table 1). Shock features are abundant in the Tissint meteorite as previously described in Baziotis et al. (2013).

Compared with other members in the depleted group of shergottites, the texture of the Tissint meteorite is more similar to those of Dho 019, DaG 475, SaU 005, and NWA 1195, with a groundmass of fine-grained olivine, pyroxene, and maskelynite, compared to those of Y-980459 and NWA 5789, which display a groundmass of olivine and pyroxene microlites within glass (Table 1).

Olivine

The olivine grains show brown coloration, typical of shergottites (produced by a dispersion of small Fe-Ti oxide inclusions, e.g., Treiman et al. 2007; Pieters et al. 2008; Bläß et al. 2010). Individual euhedral grains reach ~1.5 mm in length, and sometimes display fragmented or skeletal textures (Figs. 2b and 2c). Olivine clusters typically are ~1 × 3 mm in size, with individual grains in the cluster varying from 0.5 to 1 mm (e.g., Fig. 2a). One of the grains in the cluster in Fig. 2a shows a curved contact with other grains. Smaller grains (<0.2 mm) in the matrix are subhedral to euhedral.

Compositions of olivine in our sections range from Fo_{81} to Fo_{35} (Table 2), comparable to the range reported by Chennaoui Aoudjehane et al. (2012) and

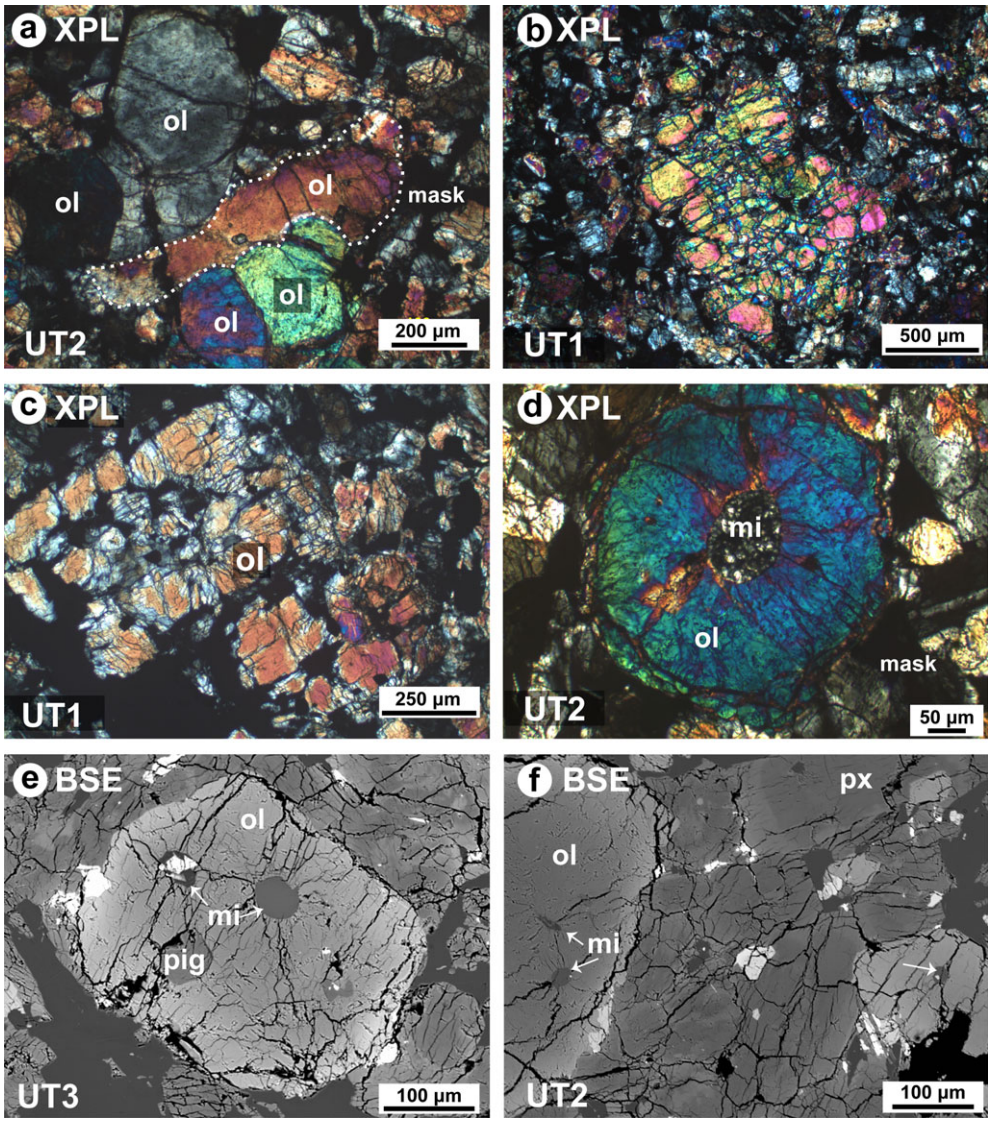

Fig. 2. Diverse olivine (ol) textures and melt inclusions (mi) in the Tissint meteorite. a) An olivine cluster shows a strongly deformed grain labeled by the dotted curve. b) A fragmented olivine grain with dark inclusions. Most fragments reach extinction simultaneously, suggesting a single crystal. c) Skeletal olivine grains showing an overall euhedral shape. d–f) Melt inclusions in olivine displaying different textures. In some olivines, both glassy and devitrified inclusions are present (arrows). The compositions of the glassy inclusions are listed in Table 1. Note the differences in scales among different figures. XPL, cross polarizers; BSE, backscattered electron image. Additional abbreviations: mask, maskelynite; px, pyroxene; pig, pigeonite.

Balta et al. (2015). Large olivines contain central regions (300–600 μm in size) of uniform composition ($Fo_{80\pm1}$), followed by concentric zoning evidenced by Fe-enrichment toward the rims (e.g., Figs. 3 and 4). Small grains in the groundmass display zoning from Fo_{54} to Fo_{33}. Balta et al. (2015) reported that the region with uniform Fo content is also surrounded by ring fractures. However, we find that the physical boundaries (ring fractures) do not coincide with the chemical boundaries between the uniform cores and the zoned rims (e.g., Figs. 1, 3, and 4). In the Fe *K*α maps of individual olivine grains, the uniform cores show no clear signs of strong resorption or rounding (Figs. 3 and 4). Moreover, the compositional transition from the uniform core to the zoned rim appears to be gradual (Figs. 3 and 4). The P *K*α maps of the olivine grains show that the uniform cores contain wide but weak (low-P) zones, and the zoned rims contain thinner oscillatory zones (Figs. 3 and 4). The P_2O_5 contents in the olivine in Fig. 4 range from below the limit of detection (0.02 wt%) in the dark zones to 0.04–0.05 wt% in the bright zones, and reaches 0.14–0.2 wt% in the brightest zones in the rim. The Cr *K*α maps of the grains show no clear zonation, but small Cr-Ti oxide

Table 1. Modal abundances of minerals and other phases in Tissint, compared with other olivine-phyric shergottites.

	Depleted									Intermediate		Enriched	
	Tissint			Y 980459	NWA 5789	DaG 478	SaU 005	NWA 5990	NWA 7032/ 7272	EETA 79001	NWA 6234	LAR 06319	Dho 019
Data sources	1	2	3	4	4	4	4	4	4	5	4	6	4
Olivine	22–26	16	25–28	8.7–26	19	10–24	22–31	25	40	7–12	35	22–25	9–14
Pyroxenes	51–60	50	50–52	48–63	38	54–65	48–58	35	35	63–69	38	54–55	61.4–65
Plagioclase	14–17	18	20–22		1–2	12–17	8.6–17	35	20	16–21	24	17.4–19.1	19.5–26.1
Oxides/sulfides	4–5	~1	1–2	0.8–1.1		1–4	~1.2			0.7–4	3	1.5–1.6	1.2–1.8
Phosphates	~1	0.5		0.5		1–1.5				1–1.7		2.1	1
Shock melt	2–4					4–7	3–7						
Mesostasis				25–37.4	41								

Data Source: 1: This study on three sections; 2: Chennaoui Aoudjehane et al. (2012); 3: Balta et al. (2015); 4: Martian Meteorite Compendium, http://curator.jsc.nasa.gov/antmet/mmc/index.cfm; 5: Liu et al. (2013); 6: Basu Sarbadhikari et al. (2009).

Table 2. Major and minor element compositions of selected minerals.

	Olivine							Fe-Cr-Ti Oxides					
	core	rim	Pyroxene			Maskelynite		crt				Merrillite	
SiO_2	39.6	32.5	54.8	50.5	48.8	51.8	53.8	0.20	0.08	0.09	0.04	SiO_2	0.06
TiO_2	<0.05	0.05	0.11	1.05	0.49	0.08	–	0.81	24.1	27.4	52.2	Al_2O_3	<0.03
Al_2O_3	0.05	0.03	0.49	1.75	0.40	30.0	28.6	7.20	7.99	3.06	0.12	La_2O_3	<0.1
V_2O_3	–	–	–	–	–	–	–	0.64	–	0.63	–	Ce_2O_3	<0.1
Cr_2O_3	0.24	<0.05	0.53	0.62	<0.05	–	–	58.7	10.1	4.72	0.48	MgO	3.33
MgO	42.6	15.5	26.9	15.5	10.1	0.16	0.15	4.91	3.83	0.89	1.93	CaO	47.1
CaO	0.22	0.39	2.05	13.6	5.69	13.5	11.6	–	0.14	0.05	<0.05	MnO	0.11
MnO	0.38	0.93	0.49	0.51	0.94	<0.05	–	0.45	0.72	0.58	0.68	FeO	2.14
FeO	17.3	50.5	15.2	16.2	32.9	0.51	0.72	27.8	52.7	60.8	43.8	Na_2O	0.59
NiO	0.12	0.05	–	–	–	<0.05	–	–	–	–	–	P_2O_5	46.5
Na_2O	–	–	<0.05	0.14	0.05	3.71	4.29	–	–	–	–	Cl	<0.05
K_2O	–	–	–	–	–	0.05	0.55	–	–	–	–		
P_2O_5	–	–	–	–	–	–	–	–	–	–	–		
S	–	–	–	–	–	–	–	–	–	–	–		
Total	100.5	99.9	100.5	99.9	99.3	99.9	99.8	100.6	99.7	98.2	99.2	Total	99.9
Mg#[a]	81	35	76	63	35	–	–	–	–	–	–		74
En	–	–	73	45	31	An 67	58	–					
Wo	–	–	4	29	13	Ab 33	39						
Oxygen	4	4	6	6	6	8	8	4	4	4	6		56
Si	1.000	0.987	1.972	1.916	1.971	2.360	2.447	0.007	0.003	0.003	0.002	Si	0.020
Ti	0.001	0.001	0.003	0.030	0.015	0.003	–	0.021	0.641	0.779	1.972	Al	0.014
Al	0.002	0.001	0.021	0.078	0.019	1.613	1.532	0.293	0.333	0.136	0.007	La	0.000
V	–	–	–	–	–	–	–	0.018	–	0.019	–	Ce	0.000
Cr	0.005	0.000	0.015	0.019	0.001	–	–	1.605	0.283	0.141	0.019	Mg	1.788
Mg	1.606	0.701	1.443	0.874	0.608	0.011	0.010	0.253	0.202	0.050	0.144	Ca	18.07
Ca	0.006	0.013	0.079	0.554	0.246	0.657	0.566	0.000	0.005	0.002	0.001	Mn	0.034
Mn	0.008	0.024	0.015	0.016	0.032	0.001	–	0.013	0.021	0.019	0.029	Fe	0.640
Fe	0.366	1.283	0.458	0.513	1.110	0.019	0.027	0.803	1.559	1.921	1.839	Na	0.408
Ni	0.002	0.001	–	–	–	0.001	–	–	–	–	–	Cl	0.005
Na	–	–	0.001	0.010	0.004	0.327	0.378	–	–	–	–	P	14.09
K	–	–	–	–	–	0.003	0.032	–	–	–	–		
P	–	–	–	–	–	–	–	–	–	–	–		
S	–	–	–	–	–	–	–	–	–	–	–		
Total	2.996	3.011	4.008	4.010	4.006	4.995	4.992	3.014	3.048	3.070	4.013	Total	35.05

[a]Mg# = molar [MgO/(MgO+FeO)]*100.

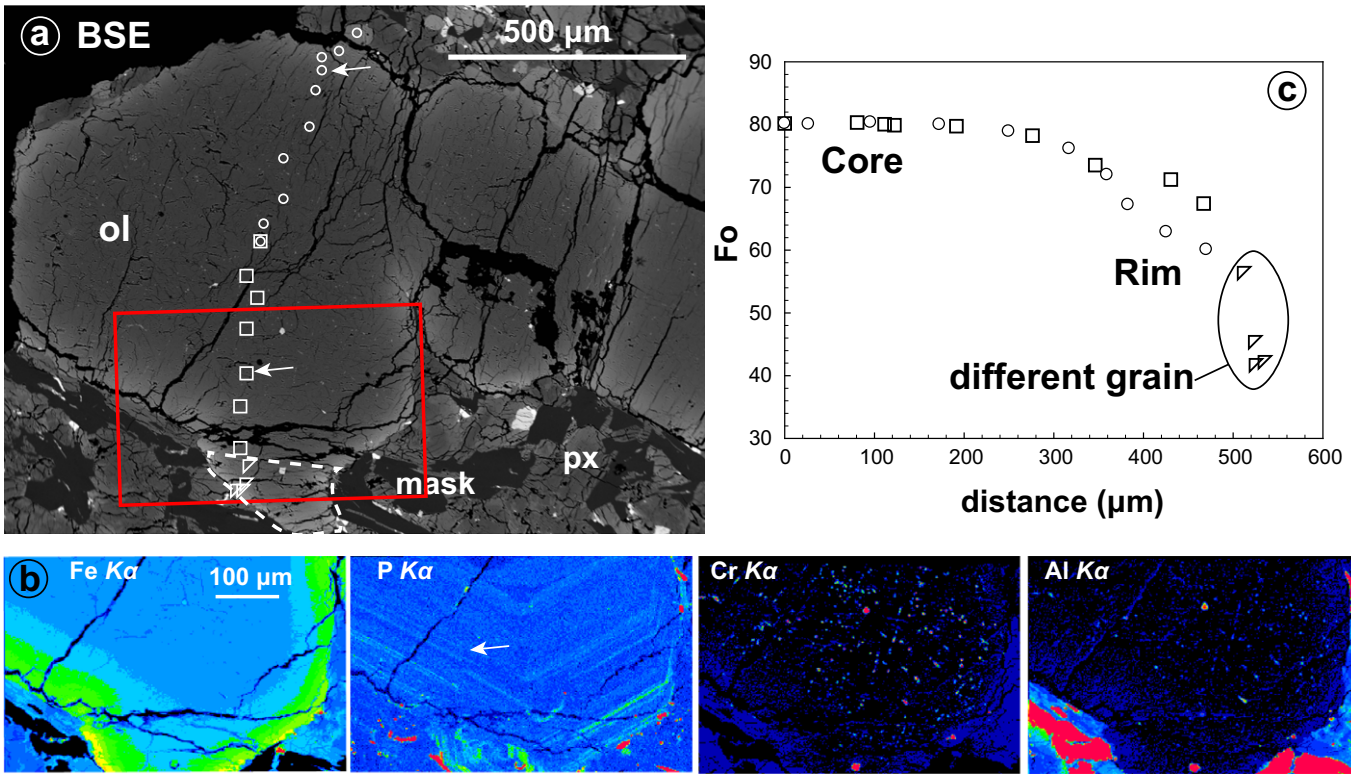

Fig. 3. BSE image, X-ray maps, and compositional zoning of an olivine megacryst in the Tissint meteorite. a) BSE image of an olivine (ol) megacryst in Tata-2-C3. Red box outlines the area of X-ray maps in (b). Locations of EMP analyses are labeled using the same symbols as in (c). Dashed curve outlines the olivine attached to the megacryst. Additional abbreviations: mask, maskelynite; px, pyroxene. b) Fe, P, Cr, and Al Kα maps of the olivine grain, showing oscillatory P zones. c) Compositional profile from the core to the rim. Triangles mark the spots on an attached olivine (different orientation). White arrows in BSE and P kα images mark olivine with Mg# 74 that is in Fe-Mg equilibrium with Mg# 76 pyroxene.

inclusions. The Al *K*α map of one olivine grain shows a broad variation of Al from below the limit of detection of 0.02 wt% at the rim to 0.06 wt% in the center (Fig. 4).

Abundances of REE in Mg-rich olivines are below the detection limits of LA-ICP-MS at our analytical conditions (see limits of detection in Table 3 and Table S1 in supporting information), similar to the finding by Balta et al. (2015), although the detection limits of REE analysis using secondary ion mass spectrometry (SIMS) were not reported. One reported olivine analysis in Table S1 in Balta et al. (2015) showed very low but apparently well-resolved REE values (8 ppb La, 23 ppb Yb, and 6 ppb Lu). In addition, we report that Tissint olivines contain significant amounts of transition group elements (Sc, V, Ti, Co, Ni). Nickel contents in olivines decrease from 910 ppm at Mg# = ~80 to 234 ppm at Mg# = ~45, whereas Co contents increase slightly from 96 to 111 ppm (Fig. 5).

Melt inclusions (round or elongated) are common in olivines (Figs. 2d–f). These inclusions are typically partially crystallized, consisting of secondary pyroxenes, feldspar, glass (Si-rich or Al-rich), and occasional chromite and sulfide, similar to melt inclusions described in other olivine-phyric shergottites (Basu Sarbadhikari et al. 2009, 2011; Liu et al. 2013). However, the Tissint olivines also contain glassy inclusions, coexisting with partially crystallized ones in the same grain (Figs. 2e and 2f), as observed in other pieces by Sonzogni and Treiman (2013). The compositions of glassy inclusions in our samples (Table 2) are significantly different from the whole-rock analysis of Chennaoui Aoudjehane et al. (2012). The glassy inclusions are noticeably higher in SiO_2 (60.9–63.4 wt%) and Al_2O_3 (12.5–13.9 wt%), and lower in MgO (1.15–1.63 wt%) and FeO (3.9–5.3 wt%), with Mg# of 30–40.

Pyroxenes

Pyroxenes occur as euhedral to subhedral grains, typically from 50 to 200 μm in width and from 0.2 to 1 mm in length. Major element compositions of all pyroxenes display a limited range from $En_{74}Wo_4$ toward $En_{\sim 52}Wo_{\sim 25}$, then to $En_{35}Wo_{13}$ (Fig. 6a). Low-Ca pyroxenes with $\sim Wo_{4-5}$ and Mg# 74–76 occur as small cores of some grains, but represent only a small

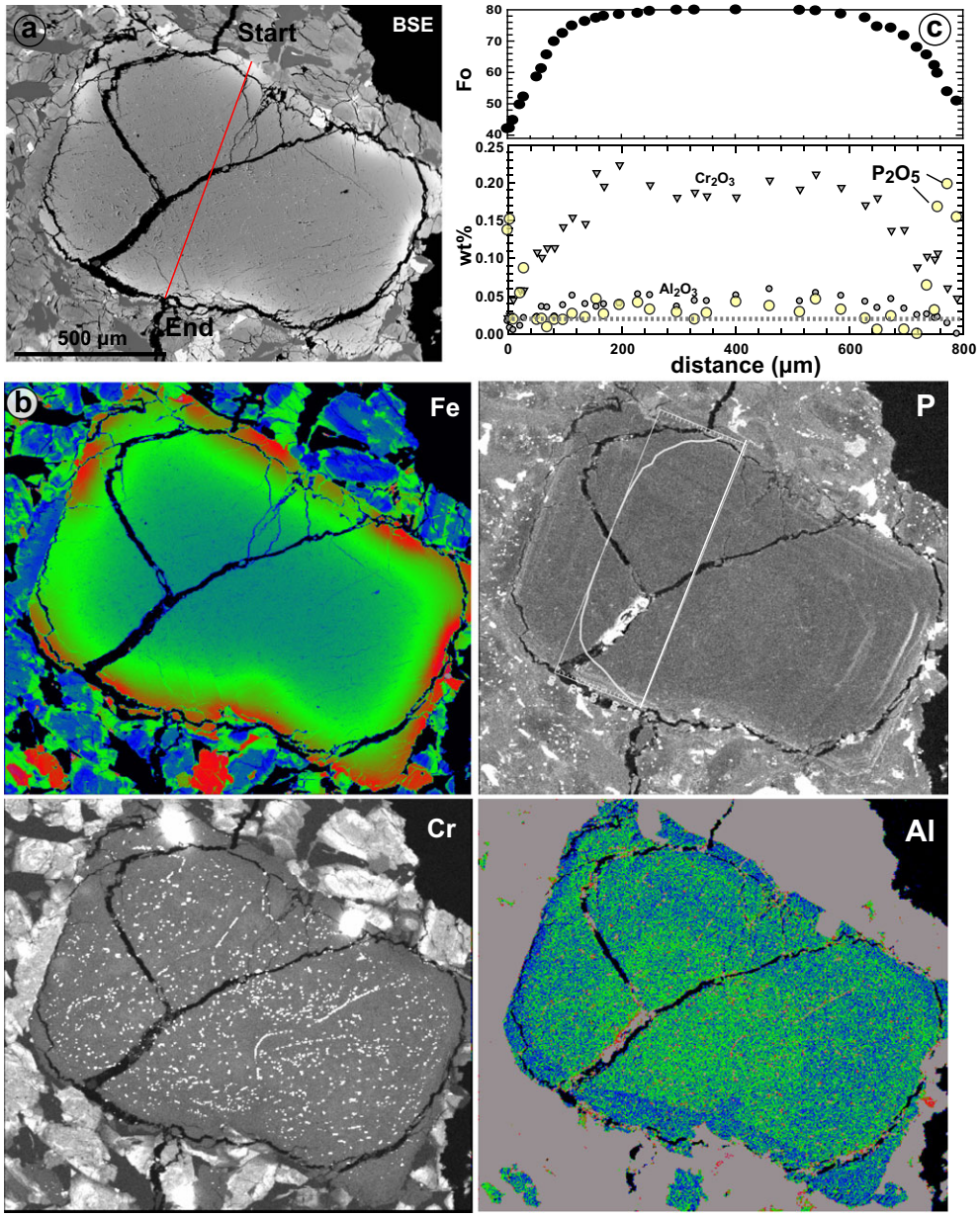

Fig. 4. BSE image, X-ray maps, and compositional zoning of an olivine megacryst in the Tissint meteorite. a) BSE image of the olivine, and red line marks the traverse of the EMP analysis. b) Fe, P, Cr, and Al Kα maps of the olivine grain, showing oscillatory P zones in the zoned Fo region, no clear P-enriched core, and subtle Al zoning. The Mg# profile was superposed on the P map. c) Concentration profiles of Mg#, P_2O_5, Al_2O_3, and Cr_2O_3 of the olivine from start (distance = 0 μm) to end (distance = ~800 μm), showing the Al_2O_3 content is below detection at the rim, and about 0.01 wt% variation between the brighter green center and darker green mantle. Dotted line shows the detection limit for P_2O_5.

proportion (5–10 vol%) of the sections studied. High-Ca pyroxene with Wo >30 is also uncommon in the Tissint meteorite (Fig. 6b), and occurs only in the interstitial regions. The TiO_2 contents in pyroxenes vary from 0.08 wt% to ~1.25 wt%, increasing with decreasing Mg#. The Al_2O_3 contents in pyroxenes vary from 0.39 to 2.83 wt%, initially increasing with decreasing Mg# from 76 to 64 and then decreasing from Mg# 64 to 35. Despite the broad chemical trend defined by multiple grains, we noticed that individual pyroxene displays different zoning patterns (normal or composite zonings, Figs. 6 and 7). The normal zoning progresses from an Mg-rich core ($En_{70}Wo_5$) to low-Ca augite rim ($En_{45}Wo_{15}$, e.g., Fig. 6). The composite zoning contains an Fe-rich pigeonite interior ($En_{50\pm1}Wo_{11\pm1}$, Mg# 56 ± 1), a Mg-rich pigeonite mantle ($En_{64}Wo_{10}$, Mg# 71), and an Fe-rich and low-Ca rim ($En_{44}Wo_{18}$, Mg# 53). X-ray maps of pyroxene grains indicate that individual

Table 3. Chemical compositions of Tissint glasses, compared to the literature data.

Ref.[a]	Fusion crust This study		Bulk rock		Groundmass		Impact melt This study		1	2	2	2	Glass inclusion		
EMP	avg (n = 73)	1σ[b]	1 bulk	1 bulk	1 gm	2 gm	avg[c] (n = 14)	1σ[b]	black gl	glass A	glass A	glassB (n = 14)	This study		
SiO_2	46.1	2.1					48.7	1.60	44.86			45.77	60.9	60.9	63.0
TiO_2	0.67	0.25	0.63	0.65	0.67		0.46	0.13	0.56			0.69	1.36	1.36	1.10
Al_2O_3	4.23	0.71	4.86	5.5	6.37		4.97	2.91	4.54			5.06	12.5	12.5	13.9
Cr_2O_3	0.53	0.20	0.44	0.78	0.7		0.91	0.52	0.81			0.66	<0.05	<0.05	0.06
MgO	18.6	1.9	17.06	17.92	15.09		15.7	2.60	19.99			16.9	1.63	1.63	1.15
CaO	6.53	0.77	6.53	7.31	7.16		8.00	1.32	6.03			7.16	15.4	15.4	13.7
MnO	0.51	0.05	0.52	0.53	0.49		0.52	0.05	0.51			0.54	0.15	0.15	0.09
FeO	19.8	2.9	21.15	20.87	18.8		19.1	2.20	21.81			20.65	5.27	5.30	4.80
NiO	< 0.05												<0.05	–	–
Na_2O	0.58	0.10	0.72	0.77	1.13		0.66	0.43	0.63			0.72	1.06	1.06	1.24
K_2O	< 0.05		0.02	0.02	0.09		<0.05		0.04				0.08	0.08	0.54
P_2O_5	0.51	0.20	0.48	0.56	0.5		0.24	0.09	0.46			0.46	1.16	1.16	1.48
S	0.08	0.11					0.21	0.14					<0.05	<0.05	<0.05
Total	98.2	0.9					99.3		100.2				99.5	98.3	99.5
Mg#	62		59	61	59		59	4	62			60	36	30	34
LA-ICP-MS[d]															
ppm	avg n = 7	1σ[b]					avg n = 13	1σ[b]					n = 1 n = 1	LOD	
Li			2.18	2	4.6	5.01				2.12	2.09				
Be				0.0314	0.0974	0.103				0.022	0.019				
K	–	–	200	235	771								1194	16.7	
Sc	–	–		39.38	36.49	34.5	–	–	38.3						
Ti	4571	701	3789	4044	3732		2,288	695					1.32	1.12	
V	217	27	194	219	205	195	236	84	200.2	256	263		79	3	
Cr	2757	476	3042	5323	4756		4,472	2169	5549				182		
Mn	4132	167					3,831	286					972.8	4.54	
Co	57.5	2	58.1	58.5	47.7	46.7	61	14	63.24	55.7	64.2	65	–		
Ni	216	15	269	262	199	197	321	136	268	238	314	304	–		
Cu	12.5	5.2	13.8	9.8	9.94	9.72	21	16.4	22.99	12.07	11		–		
Zn	86.6	3.8	63	63.2	55	59	104	18.0	87.3	62.3	66.4		52.26	0.69	
Ga	11.3	1.2	12.05	11.32	11.25	11.14	9	2.51	9.29	11.25	9.54		22.03		
Ge	1.07	0.28					3	1.66					2.02		
Rb	–	–	0.376	0.305	2.52	3.15	–	–	1.36	0.274	0.227	0.25	–		
Sr	26.3	5.0	34.78	31.79	43.4	43.17	16.90	6.37	25.07	30.99	25.52	24.60	69.6	0.147	
Y	14.3	4.6	14.91	13.22	12.82	12.17	6.169	1.47	8.21	11.42	10.35	10.49	24.67		
Zr	24.1	8.4	23.14	19.69	24.73	26.26	9.991	3.74	20.1	16.7	14.87	12.76	41.75		
Nb	0.232	0.046	0.28	0.219	0.771	0.85	0.293	0.13	0.226	0.257		0.192	–	0.103	
Ba	2.216	0.303	3.54	2.5	36.57	47.54	1.886	1.08	5.91	2.04	1.9	1.330	4.502	0.049	

Table 3. *Continued*. Chemical compositions of Tissint glasses, compared to the literature data.

LA-ICP-MS[d]														
ppm	avg $n = 7$	1σ[b]					avg $n = 13$	1σ[b]					$n = 1$ $n = 1$	LOD
La	0.397	0.112	0.315	0.283	2.62	2.43	0.169	0.07	1.2	0.258	0.242	0.216	0.618	0.113
Ce	1.142	0.108	1.16	0.945	6.19	5.7	0.574	0.30	2.81	0.897	0.816	0.767	2.064	1.102
Pr	0.204	0.071	0.237	0.192	0.745	0.693	0.103	0.05	0.324	0.175	0.162	0.153	0.283	0.580
Nd	1.655	0.425	1.63	1.37	3.37	3.07	0.941	0.32	1.58	1.27	1.18	1.100	2.758	0.129
Sm	1.104	0.342	1.07	0.877	1.13	1.08	0.514	0.27	0.673	0.806	0.744	0.705	2.701	0.457
Eu	0.420	0.079	0.503	0.405	0.452	0.425	0.211	0.07	0.271	0.382	0.348	0.325	0.478	0.228
Gd	1.952	0.443	1.85	1.7	1.79	1.73	0.961	0.35	1.05	1.59	1.52	1.450	2.732	0.453
Tb	0.427	0.171	0.364	0.333	0.331	0.323	0.181	0.06	0.196	0.319	0.295	0.282	0.855	0.079
Dy	2.751	1.018	2.38	2.22	2.17	2.16	1.213	0.35	1.24	2.14	2.08	1.870	4.897	0.222
Ho	0.495	0.200	0.504	0.466	0.453	0.447	0.262	0.09	0.266	0.442	0.434	0.401	1.054	0.135
Er	1.606	0.574	1.48	1.3	1.24	1.24	0.749	0.22	0.764	1.26	1.23	1.110	1.785	0.353
Tm	0.201	0.087	0.204				0.117	0.03					0.610	0.630
Yb	1.557	0.447	1.3	1.17	1.1	1.12	0.750	0.25	0.772	1.12	1.09	1.000	1.886	0.364
Lu	–	–	0.19	0.16	0.15	0.162	0.194	0.06	0.11	0.161	0.155	0.147	–	0.117
Hf	0.932	0.359	1.01	0.81	0.96	0.98	0.451	0.17	0.67	0.77	0.72	0.640	1.448	0.365
Ta	0.048	0.008		0.0138	0.0533	0.057	–	–		0.011	0.015	0.01	–	0.333
W	0.207	0.030		0.041	0.094	0.095	–	–					–	0.254
Au	0.123	0.056					–	–					–	
Pb	–	–	0.25	0.15	0.74	0.75	–	–		<0.05	0.08	0.13		
Th	–	–		0.024	0.915	0.715	–	–	0.323	0.0184	0.02	0.0159		
U	–	–		0.007	0.1002	0.134	–	–	0.123	0.0050	0.0055	0.0054		

[a]References (Ref) are: (1) Chennaoui Aoudjehane et al. (2012); (2) Barrat et al. (2014). Note Th and U data in Chennaoui Aoudjehane et al. (2012) are switched (see the corrected order in Barrat et al. 2014).

[b]1σ is 1 standard deviation of the average.

[c]Average of impact melt in our study only included the glassy regions of the impact melt pockets.

[d]Average of a number of LA-ICP-MS analysis. LOD is the limit of detection estimated based on background counts to 3σ confidence interval.

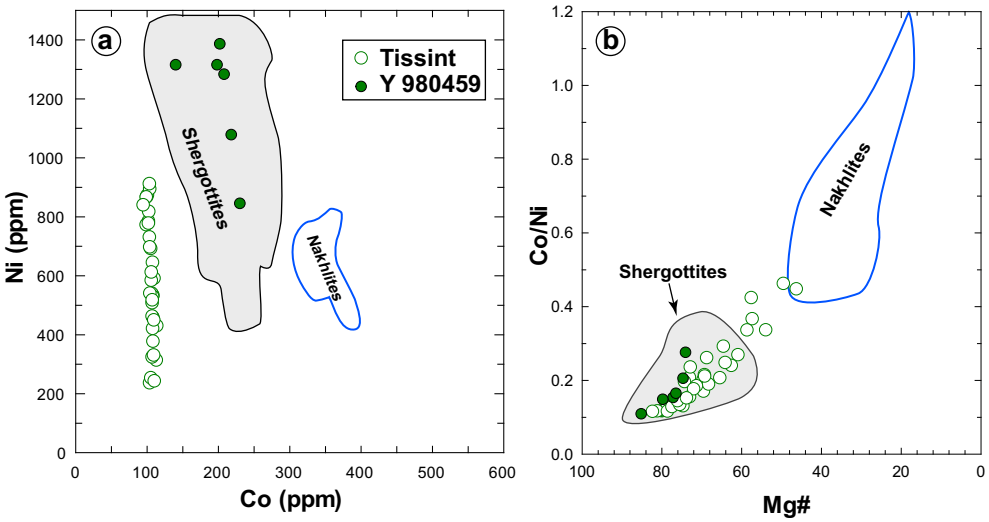

Fig. 5. a) Co and Ni contents of olivine, and fields redrawn from Shearer et al. (2008). b) Co/Ni values as a function of Mg# of olivine. The fields for other shergottites and nakhlites are from Papike et al. (2009). Data for Y 980459 are from Usui et al. (2008).

pyroxene grains display highly irregular Ca zoning (Fig. 7).

As in the olivines, Co contents of pyroxenes show small variations (39–52 ppm), whereas Ni contents show a large decrease with decreasing Mg# (~180 to 55 ppm). Contents of REE in Ca-poor pyroxenes are below detection limits of LA-ICP-MS (Table 3 and 4), much the same as observed with SIMS analysis by Balta et al. (2015). The REE patterns of augites (Table 3, and Fig. S1 in supporting information) are comparable to those in maskelynite, except for Eu. Other detectable incompatible elements display an increase in abundances with decreasing Mg# (Fig. S1).

Maskelynite

All plagioclase grains originally present in the Tissint meteorite have been converted by shock to isotropic maskelynite and melt-glass. Maskelynite comprises 14–17 vol% of our sections. These grains generally maintain their elongated shapes, but shock has rendered the distinction among individual grains difficult. Compositions of maskelynite display a limited range from $An_{67}Or_{0.2}$ to $An_{55}Or_3$ (Table 2), smaller than the range ($An_{68}Or_1$–$An_{47}Or_5$) reported by Balta et al. (2015). There are minor but significant amounts of FeO (0.48–1.42 wt%), the largest amounts possibly indicating actual melt-glass rather than solid-state transformed maskelynite. In addition to Fe, maskelynite contains variable amounts of Ti (250–450 ppm), V (1.6–4.3 ppm), Mn (60–74 ppm), Sr (120–169 ppm), and Ba (1.6–4.4 ppm), with no clear correlations with An contents. Abundances of REE (except for Eu) of most maskelynites are below detection limits of LA-ICP-MS analysis, except for one point (Table S1). It is possible that this point may have sampled a tiny phosphate grain trapped between original grain boundaries, as observed in Chen et al. (2015). The REE abundances in maskelynite obtained using SIMS by Balta et al. (2015) are <20 ppb, below detection limits of LA-ICP-MS.

Oxides

Chromite occurs as euhedral grains in the rim of olivine (~Fo_{76}), but not in the uniformly Mg-rich cores (Table 2). The lack of chromite inclusions in olivine cores is also reported in other Tissint samples (Balta et al. 2015). Isolated Cr-Ti spinels in the groundmass are zoned from chromite cores to Ti-chromite mantles to nearly-pureulvöspinel rims (Table 2, Fig. S2 in supporting information). This zonation is shown using Cr# = molar Cr/(Cr+2Ti+Al)*100 in Fig. S2. The compositions of the cores are 84–80 mole% Cr#, 2–6 mole% Ti# (Ti# = molar 2Ti/[Cr + 2Ti + Al]*100), and Mg# of 37–11, and the rims are ~8 mole% Cr# and ~85 mole% Ti#. The transition from chromite to ulvöspinel occurs at Mg# ~10. Ilmenite occurs as individual, subhedral to euhedral, lath-shaped grains in the matrix. Ilmenite in the Tissint meteorite contains 1.65–2.29 wt% MgO and 0.15–0.65 wt% Cr_2O_3 (Table 2). The MgO and Cr_2O_3 contents of ilmenite display a positive correlation, although there is considerable scatter.

Phosphate

Phosphate minerals comprise ~1 vol% of the whole-rock. We observed only sodium-merrillite, similar to Balta

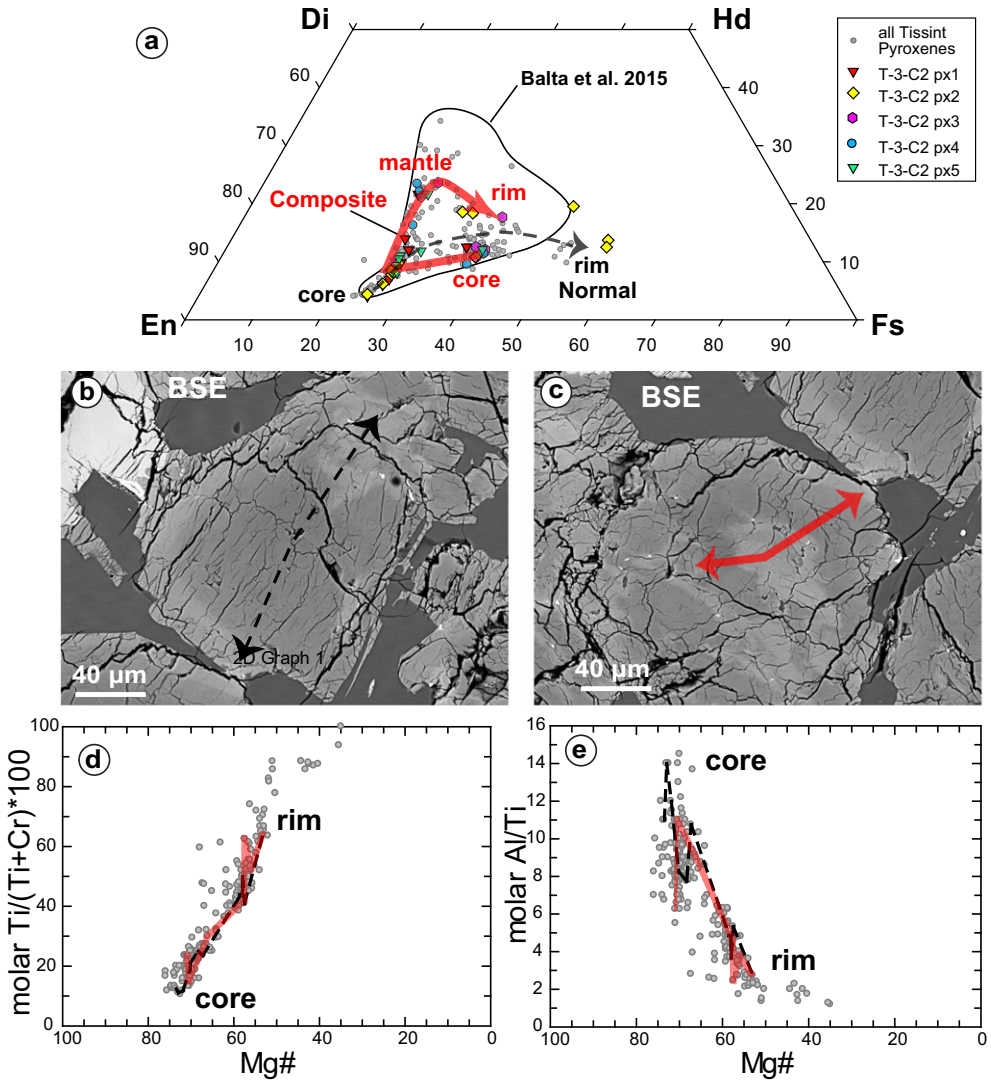

Fig. 6. Pyroxenes in the Tissint meteorite. a) Compositions of all pyroxenes analyzed, and the individual grains (as individual symbols) in section Tata-3-C2. The red and blue curves represent the compositional trends of a composite- (c) and a normally (b) zoned pyroxene, respectively. Arrows represent the rim compositions. Dashed curve represents compositions of other grains trending toward a more Fe-rich rim. b, c) BSE images of the normal and composite zoned pyroxenes in Tata-3-C2 plotted in (a). d) Correlation of molar Ti*100/(Ti+Cr) in pyroxenes. Increasing molar Ti/(Ti+Cr) with decreasing Mg# indicates that crystallization removes more Cr than Ti, until pyroxene with an Mg# 50 begins to precipitate, at which point ilmenite appears on the liquidus. e) Molar Al/Ti as a function of Mg# in pyroxenes. Blue and red lines correspond to those in (a–c). The initial rapid decrease in Al from Mg# 76–60 is caused by absence of plagioclase. At Mg# ~60, the appearance of plagioclase causes the molar concentration of Al in pyroxene to decrease.

et al. (2015). The major constituents of merrillite give an average formula of $(Na_{0.54–0.46})(Mg_{1.28}Mn_{0.05}Fe_{1.03})Ca_{18.1}(PO_4)_{14}$, with a notable deficiency in the Na site. The compositional ranges in merrillites in our samples are slightly greater in FeO (2.1–5.4 wt%, Table 2) versus 2.4–4.9 wt% (Balta et al. 2015). The formula moles of Na and Mn per 56 oxygen and Mg# of Tissint merrillites are intermediate between other depleted shergottites (Fig. 8). This large range of compositions among different grains is typical for Martian merrillites (e.g., Shearer et al. 2011, 2015).

The merrillites are rich in rare earth elements (La-Gd: ~14–345 ppm; Tb-Lu: 18–414 ppm; Table 3) as previously reported by Balta et al. (2015). However, CI-chondrite-normalized REE patterns of merrillite are characterized by strong LREE depletion, with CI-chondrite-normalized La/Sm values ($[La/Sm]_N$) of 0.16–0.23, and $(La/Yb)_N$ of 0.18–0.23 (Fig. 9). Merrillite grains also contain negative Eu anomalies ($Eu/Eu^* = Eu_N/[Sm_N^* Gd_N]^{0.5}$) of ~0.55–0.60, and slight to moderate HREE depletion ($[Gd/Yb]_N$ ranging from 1.54 to 1.79) (Fig. 9).

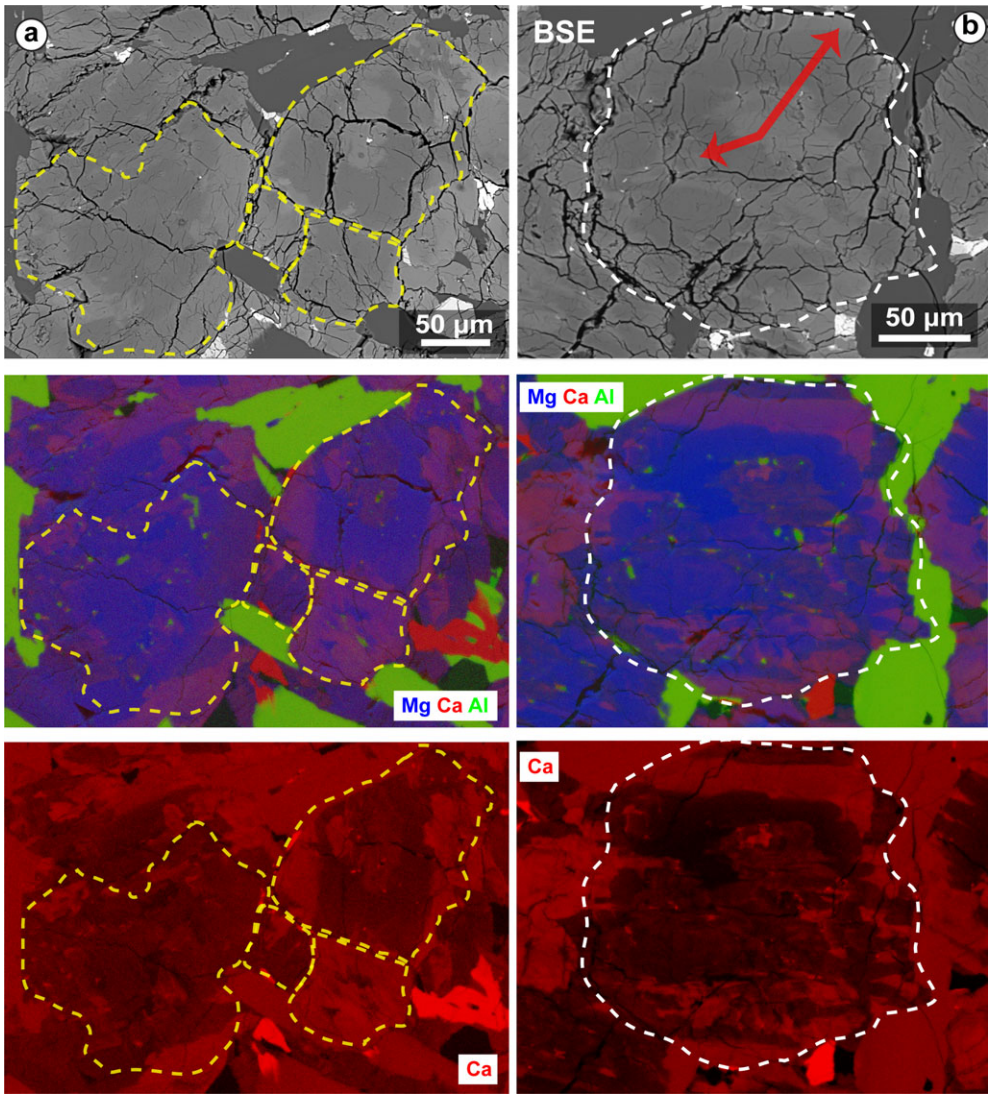

Fig. 7. BSE and X-ray maps showing compositional zoning in groundmass pyroxenes in the Tissint meteorite. Dashed lines outline single crystals based on optical microscope observations. Abbreviations: mask, maskelynite; merr, merrillite; px, pyroxene.

Fusion Crust

Our chips are covered with a thin layer (up to ~50 µm thick) of bubbly fusion crust. The composition of the fusion crust shows that SiO_2 and Al_2O_3 contents range from 44.3 to 48.6 wt% and 3.5 to 6.0 wt%, respectively. The average composition of 73 analyses of the fusion crust displays a basaltic composition with Mg# of 62 (Tables 2 and 3), similar to the bulk-rock data of Chennaoui Aoudjehane et al. (2012) (Table 3). The REE abundances of different analyses of the fusion crust span the bulk rock values reported in Chennaoui Aoudjehane et al. (2012) (Fig. 10a), and the average REE abundances of all fusion crust analyses are similar to the bulk rock data (Fig. 10c). Normalized to the CI chondrite values, LREE values of the fusion crust are highly depleted relative to HREE (La/Yb_N = 0.1–0.22, Fig. 10a), similar to the merrillite data; this suggests that this sample does belong to the depleted shergottite group. The fusion crust analyses also display Eu anomalies (Eu/Eu*) of mainly 0.7–0.95 with one datum of 1.16. In the extended trace element plot, the fusion crust displays weak depletions in Ti and Nd, relative to neighboring elements (Fig. S3 in supporting information).

Shock-Induced Melts (Now Glass)

Shock-induced melt veins are typically ~1 µm to tens of µm in width. These veins are generally filled with microcrystals in an interstitial glass. Near the fusion crust of UT1, a shock melt vein was observed

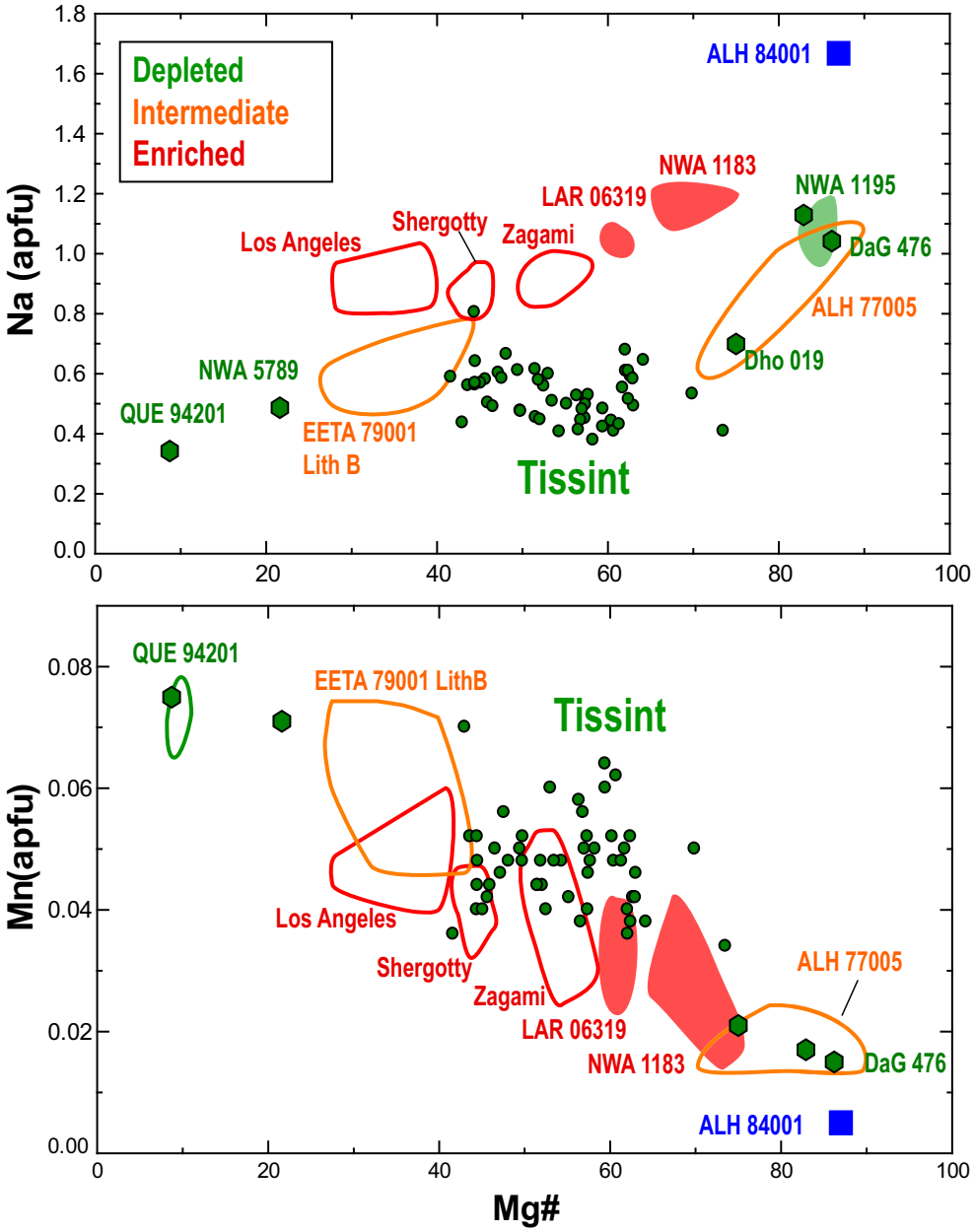

Fig. 8. Compositional variations of merrillite in Tissint, in comparison with other samples. Na and Mn are expressed as number of atoms per formula unit (a.p.f.u.), which is calculated on a basis of 56 O. Data for other samples are from Jolliff et al. (2006) and Shearer et al. (2015). Different colors are used to distinguish different chemical groups.

with relatively clear and homogeneous yellow–green glass, and serial-cut sections demonstrate that this melt vein connects to a large melt pocket.

Shock-formed melt pockets range in size from 20 μm to 1 mm in diameter in our sections (Baziotis et al. 2013; Ma et al. 2014; Chen et al. 2015). Five serial-cut sections show that some of the pockets extend to 1 mm in the third dimension. These rounded pockets predominantly exist between the interface of olivine and other minerals, and are heterogeneous in their textures and mineral constituents (Fig. 11). Many pockets display a glassy center that typically lacks crystalline phases, but do contain small FeS droplets.

The major and minor element compositions of the glassy regions are generally basaltic (Table 3). Trace elements were obtained on both glassy and crystalline regions. The REE abundances of different pockets range by a factor of 3–4 for a given element, comparable to the range observed in pyroxene and maskelynite (Fig. 10b). The upper range of our data is

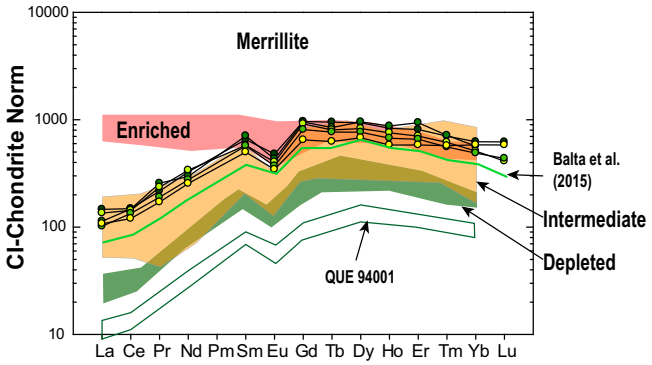

Fig. 9. The REE abundances in Tissint merrillite normalized using those in CI chondrite of Anders and Grevesse (1989), and compared to results reported by Balta et al. (2015), and to those in different chemical groups of shergottites from Shearer et al. (2011, 2015).

similar to those reported by Barrat et al. (2014). The CI-chondrite-normalized REE patterns of pockets still show the strong LREE depletion relative to HREE (La/Yb_N = 0.09–0.2, Fig. 10b). The Eu anomalies vary from negative to positive values (Eu/Eu* = 0.53 to 1.97).

DISCUSSION

Nature of the Olivine Megacrysts: Xenocrysts, Phenocrysts, or Antecrysts?

Understanding the nature of olivine and sometimes orthopyroxene megacrysts is required to assess whether the samples represent melt compositions because olivine-phyric shergottites are typically the most primitive members of the basaltic Martian meteorites. In the current study, we apply the nongenetic term megacryst to all of the large grains >200–600 μm in length, following the criterion of Gross et al. (2011). Megacrysts may have three origins: phenocryst, antecryst, or xenocryst. If a megacryst in a rock is a phenocryst, it implies that the megacryst crystallized from the melt that formed the rock. Xenocryst in terrestrial usage usually implies nonmagmatic sources, such as a piece of wall rocks that is incorporated into the magma (e.g., Davidson et al. 2007). An antecryst is also a xenocryst, but it grew from an earlier, typically more primitive, melt associated with the same magmatic system and was reincorporated into the later magma (e.g., Davidson et al. 2007; Jerram and Martin 2008; Vinet and Higgins 2010). In particular, the term antecryst was used to classify deformed olivines in Hawaiian lavas that are interpreted to have been cumulates from earlier magmas of a single magmatic system, but are unrelated to the melt in which they were ultimately found (e.g., Jerram and Martin 2008; Vinet and Higgins 2010). For the Tissint case, Balta et al. (2015) referred to the uniform Mg# cores of olivine megacrysts as antecrysts, thereby arguing that they formed in the same active magmatic system as their host rock, but were later incorporated into their final host magma after settling, accumulation, and re-entrainment.

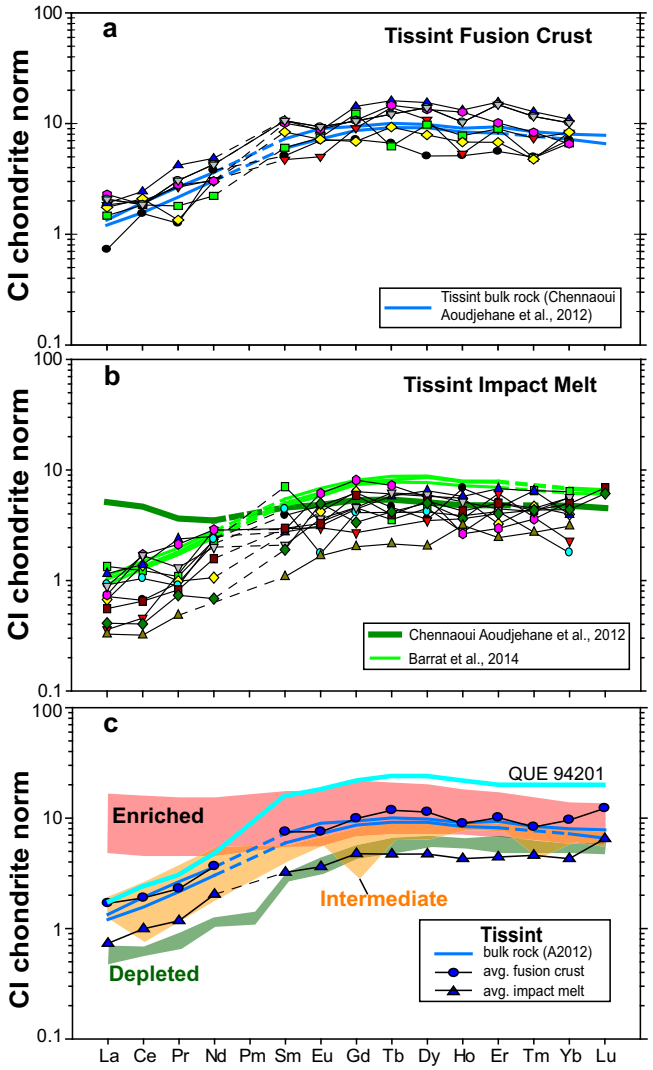

Fig. 10. The REE abundances in Tissint glasses normalized to those in CI chondrite of Anders and Grevesse (1989). a) REE in fusion crust from this study compared to whole-rock data from Chennaoui Aoudjehane et al. (2012). Whole-rock data from Balta et al. (2015) are identical to those from Chennaoui Aoudjehane et al. (2012), and thus are omitted for clarity. b) REE abundances in impact melts in this study, compared to those reported by Chennaoui Aoudjehane et al. (2012) and Barrat et al. (2014). c) Average fusion crust and average impact melt compositions are compared to whole-rock data (A2012) of Chennaoui Aoudjehane et al. (2012) and the overall ranges of chemical groups. Data sources for the fields of enriched, intermediate, and depleted groups are compiled in Liu et al. (2013). Missing values are marked by dashed lines.

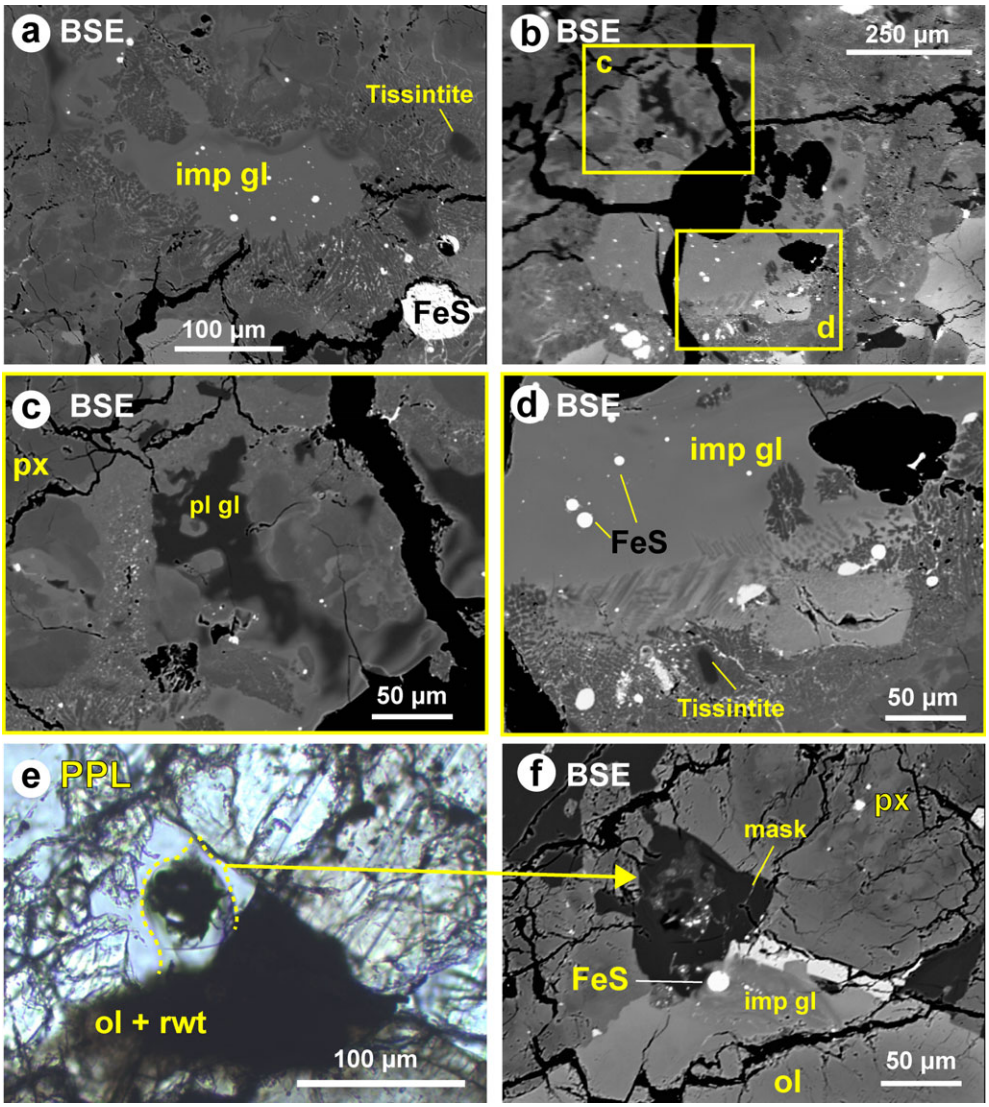

Fig. 11. Shock-formed melts in Tissint showing diverse textures. a–d) The glassy interior with FeS droplets, surrounded by microcrystals and rimmed by primary minerals. b) A bubble-bearing pocket. Two areas marked by squares are shown in (c) and (d) at higher magnifications. e) Transmitted light (PPL, plane-polarized light) and (f) BSE of the same area, showing a small plume (dashed line for boundary) from a melt pocket injected into the maskelynite (mask). ol, olivine; px, pyroxene; rwt, ringwoodite; imp gl, shock-formed glass; pl gl, glass with plagioclase-like composition.

Xenocrystic megacrysts are typically identified using either Fe-Mg disequilibrium between the megacryst and whole-rock or trace element abundance contrasts between olivine-hosted melt inclusions and whole-rock (e.g., EETA 79001 lithology A, McSween and Jarosewich 1983; Liu et al. 2013; Dar al Gani 476, Mikouchi et al. 2001; LAR 06319, Basu Sarbadhikari et al. 2009, 2011). In contrast, it may not be possible to distinguish between antecryst and phenocryst if they formed from melts of similar composition. To complicate the issue, a single megacryst may be composed of a xenocrystic or antecrystic interior overgrown by a phenocrystic rim (e.g., EETA 79001, Liu et al. 2013). The interpretation of Balta et al. (2015) that the olivine cores in Tissint represent antecrysts is based on the observation that the uniform Mg# cores are surrounded by a normally zoned, Fe-rich rims, as well as the higher modal abundance of olivine in Tissint compared to other shergottites that lack accumulated olivine.

We evaluate the nature of olivine megacrysts in Tissint using various approaches. First, olivine with an Mg# of 83 or 80 would be in equilibrium with the whole-rock (Mg# 59–60, Chennaoui Aoudjehane et al. 2012), calculated using K_D (=$[Fe/Mg]_{ol}/[Fe/Mg]_{melt}$) of 0.3 or 0.35, respectively (Longhi and Pan 1989;

Goodrich 2003; Filiberto and Dasgupta 2011). The olivine cores of Mg# of ~81 in our samples and other sections (Chennaoui Aoudjehane et al. 2012; Balta et al. 2015) fall in the range of the calculated values, which argues against a xenocrystic origin for the olivine cores.

Second, the distributions of certain trace elements (e.g., Ni, Co, Sc, V, Y) between olivine cores and whole-rock may be used to assess the origin of the olivine megacrysts. The Ni and Co distributions between olivine and melt were experimentally determined for Martian conditions (Filiberto et al. 2009; Herd et al. 2009) and lunar conditions (Longhi et al. 2010). Despite some scatter among experimental results, Longhi et al. (2010) concluded that the experimental data can be fit within the specified errors with the formulation of Beattie et al. (1991):

$$D_{Ni} = D_{MgO} \times 3.346 - 3.665, 1\text{standard error of } 1.956;$$

$$D_{Co} = D_{MgO} \times 0.786 - 0.385, 1\text{standard error of } 0.233;$$

where D is the cation mole ratio of Ni, Co, or MgO between olivine and melt. From the above relationships, the calculated D_{Ni} and D_{Co} values are 4.3 and 1.5, respectively, using the composition of olivine cores and the whole-rock composition of Chennaoui Aoudjehane et al. (2012). The measured Ni and Co contents in olivine cores, divided by whole-rock Ni and Co concentrations, yield D_{Ni} and D_{Co} of 3.3 and 1.7, which agree with the calculated values within stated errors above (1.956 and 0.233, respectively).

Third, in contrast to the suggestion of Balta et al. (2015) that the modal abundance of olivine is anomalously high, we find that the olivine abundances in Tissint are similar to many other olivine-phyric shergottites, with or without accumulated olivine (Table 1). Moreover, Peters et al. (2015) reported that REE abundances of olivine-hosted melt inclusions in the Tissint meteorite are similar to those of the whole-rock. These similar REE contents suggest that olivine cores in the megacrysts grew from a melt similar to that which formed the Tissint meteorite, consistent with the inferences that the melt-inclusion-bearing olivine grains are phenocrysts and that the amount of xenocrystic (including antecrystic) olivine is minute at best.

Fourth, antecrystic olivines formed in an earlier phase of the magmatic system would most likely have been normally zoned in Mg# at the time of their formation. For a Fe-Mg-zoned olivine up to 600 μm in diameter (e.g., the grain shown in Fig. 3) to homogenize via Fe-Mg diffusion, it would require about 100–200 years at 1100 °C using the Fe-Mg diffusion coefficients of Jurewicz and Watson (1988) or Dohmen and Chakraborty (2007). This requires that diffusive equilibration occurs while the magma is actively cooling and crystallizing in the Martian crust. While we cannot rule out this possibility, in the absence of constraints on magma-flux and magma-chamber depth, the antecryst concept is poorly substantiated, especially versus the phenocryst model presented below.

Fifth, phosphorus zoning of olivine grains provides a proxy for the early crystallization history of basaltic magma (Milman-Barris et al. 2008). The P zoning of olivine megacrysts in three olivine-phyric shergottites has been used to evaluate the nature of megacrysts (Peslier et al. 2010; Shearer et al. 2013). These studies show that the antecrystic/xenocrystic portions of the olivine grains tend to show rounding in P Kα maps, whereas phenocrystic olivine grains do not contain distinctive cores in P Kα maps. Our limited data shown in Figs. 3 and 4 indicate that the homogeneous Mg# regions display weak oscillatory P zoning, transitioning to strongly oscillatory growth zoning in the rims without rounding or evidence of resorption. This is consistent with a phenocrystic origin. The Fe Kα maps of different sections show that the uniform Mg# cores of most olivine megacrysts have shapes similar to the whole grains (Fig. 1). Two grains in the olivine cluster in UT3 contain irregularly shaped cores (marked by white arrows), which could be caused by merging of multiple grains within a single overgrowth mantle and presence of highly strained olivine as in Fig. 2a. However, it could also indicate that a small population of the olivine does contain antecrystic cores.

Based on the above discussion, we conclude that the olivine megacrysts in Tissint are mostly phenocrysts. However, it is not possible to categorically reject the antecryst hypothesis because an ad hoc mixture of antecryst grains and an unknown composition of the initial melt can always be proposed to make up a whole-rock chemistry. In the absence of evidence *requiring* disequilibrium within the rock, however, another possible explanation of uniform olivine cores is that they formed by equilibrium crystallization from the initial melt, which requires a hot magma body with a relatively slow cooling rate. Such a model can be tested, and below, we consider the possibility that olivines in Tissint are phenocrysts, with the uniform cores formed by equilibrium crystallization, and the rims formed by subsequent fractional crystallization.

Crystallization History of Tissint

Observed Sequence

The crystallization history of a rock can be inferred from mineral chemistry and petrographic observations. As discussed above, the most Mg-rich olivines are likely

phenocrysts. The uniform olivine cores suggest that the early olivine may have grown slowly under equilibrium conditions. Such conditions are likely achieved while the fraction of olivine was small and the magma was near its liquidus temperature (slow cooling). With continuing, perhaps accelerated, cooling and crystallization, the olivine mantles started to form. The concentration profiles between the uniform core and the rim can form under a cooling rate of 0.2 °C h^{-1}, using the olivine geospeedometer of Taylor et al. (1977).

Olivines of Mg# 81–74 are more Mg-rich than those in equilibrium with the most Mg-rich pyroxene (Mg# 76, Wo_4) in the Tissint meteorite, indicting a protracted phase of fractional crystallization of olivine before saturation of the magma with pyroxene. Pyroxenes of Mg# 76 would be in equilibrium with olivine of Mg# 74 using $K_{D,Ol-cpx}^{Fe-Mg}$ of 1.1–1.2 (Longhi and Pan 1989; Filiberto et al. 2010). Multiple pyroxene grains display compositional trends from Mg# 76 pyroxene to augite to Fe-rich pigeonite (Fig. 6a). However, individual pyroxenes in the Tissint meteorite display different types of zonation (normal, reverse, or oscillatory). It is unclear if this reflects changes in magma conditions (e.g., melt composition, or f_{H2O}), recharge events, or kinetic factors (such as growth mode). Cation fraction of Ti in pyroxene increases, whereas Cr content in pyroxene decreases with decreasing Mg# in pyroxene, suggesting that chromite was crystallizing contemporaneously with pyroxene. The presence of large Ti-chromite only in olivine mantles or rims and Cr-ulvöspinels in the matrix are consistent with the deduction from mineral chemistry. Plagioclase joins the crystallization sequence when the pyroxene Mg# decreases to ~65, as shown by a maximum in the Al/Ti–Mg# correlation in pyroxenes (Fig. 6d). The low Na content and the negative Eu anomaly of merrillite are consistent with its formation after plagioclase crystallization, a conclusion similar to that stated by Shearer et al. (2015).

Together, the petrographic observations and mineral chemistry of the Tissint meteorite are consistent with the following crystallization sequence: olivine (Mg# 81 ± 1) → olivine (Mg# 76) + Ti-chromite → olivine (Mg# 74) + Ti-chromite → olivine (Mg# 74–63) + pyroxene (Mg# 76–65) + Cr-ulvöspinel → olivine (Mg# 63–35) + pyroxene (Mg# 65–60) + plagioclase, finally followed by late-stage ilmenite and phosphates. On the basis of the uniform olivine cores, the early stage may have occurred under equilibrium conditions, followed by fractional crystallization, which is modeled below.

MELTS Modeling

The crystallization history of Tissint was simulated using the alphaMELTS software (http://magmasource.caltech.edu), a flexible text-menu or scriptable driver for subroutine versions of the algorithms MELTS, pMELTS, and pHMELTS; this also has added capability for tracking the behavior of trace elements (Ghiorso and Sack 1995; Asimow and Ghiorso 1998; Asimow 1999; Asimow et al. 2001, 2004; Ghiorso et al. 2002; Smith and Asimow 2005). The original MELTS calibration emphasizes low-P experimental data on mafic systems and is most suitable for modeling Tissint crystallization (Balta and McSween 2013). The MELTS modeling of Tissint is conducted in two stages 1) equilibrium crystallization (EC) during isobaric cooling from the liquidus down to a selected transition temperature where Fo_{81} forms; 2) fractional crystallization (FC) (beginning with the residual liquid composition at the end of the EC stage). We used the average bulk rock composition reported by Chennaoui Aoudjehane et al. (2012; their Table S7, columns 1 and 2) as initial bulk composition, although in the end we found it necessary to adjust the Cr_2O_3 and H_2O contents from their nominal values. That is, we consider the entire evolution to happen in a closed system, with the onset of fractional crystallization caused by cooling becoming rapid compared to diffusive equilibration of crystals rather than by physical separation of the crystals. Both stages are calculated by decreasing temperature in 1 °C increments. An exhaustive search of parameter space of such two-stage models is impractical and MELTS has artifacts and incomplete treatment of some phases (e.g., Na-merrillite is absent from the model) such that there is a risk of overfitting in a blind parameter search. Therefore, we based our initial guesses of parameters on observations.

For the EC stage, we use an oxygen fugacity of QFM−3.6 to be consistent with the reported values for the early crystallizing phases (e.g., Castle and Herd 2014; Balta et al. 2015). The pressure for the EC stage is not critical as long as it is sufficiently low that orthopyroxene will not be the liquidus phase. For our simulation, we choose 65 MPa. Because only olivine formed in the EC stage, we run the simulation from the liquidus temperature (1418 °C) to the temperature (1354 °C) at which olivine composition becomes Fo_{81}. The model predicts ~11% olivine of Fo_{81} formed during the EC stage. Based on the size of the uniform cores (Figs. 3 and 4), they make up ~40 vol% of the total olivine, which equals about 8–10 vol% of the bulk samples. The predicted amount is broadly similar to the observed mode.

For the FC stage, optimized conditions include progressive decrease in pressure from 65 MPa to 0.1 MPa, variable oxygen fugacities (QFM−3.6 to −4.3), and a starting temperature of 1352 °C. The polybaric simulation path allows the olivine–pyroxene peritectic to shift along with the evolving liquid

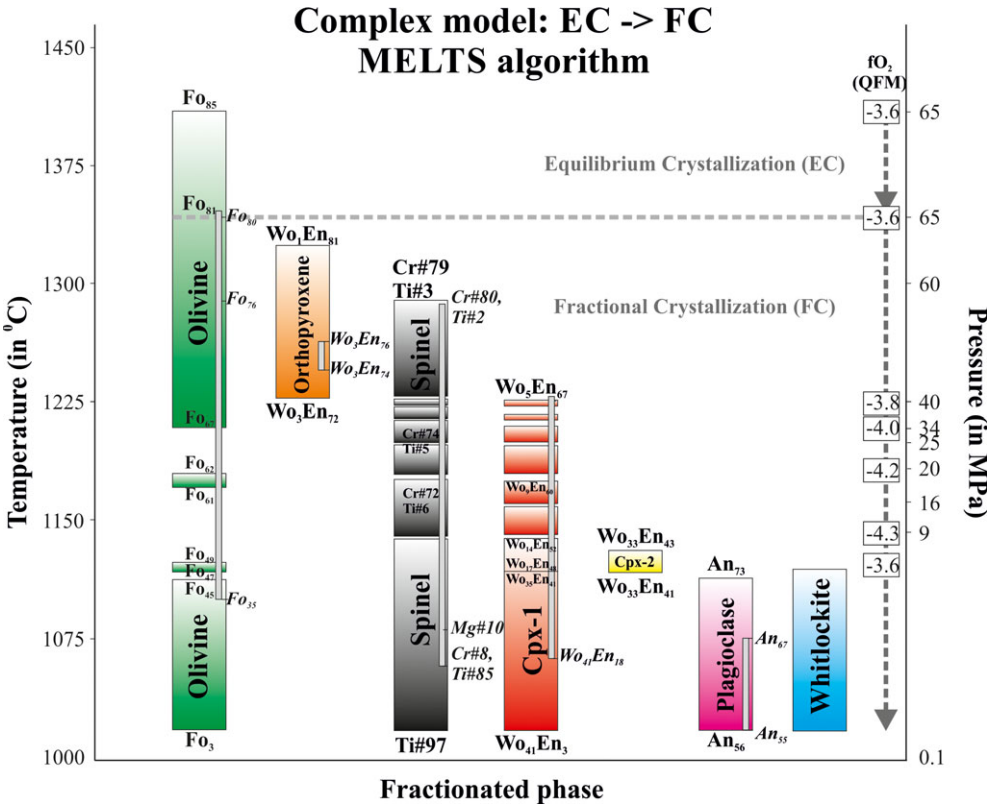

Fig. 12. Comparison of crystallization history predicted by the MELTS model (Calc., wide vertical bars) with observed mineral compositions (narrow gray bars). Based on the observed crystallization sequence and inferred initial equilibrium crystallization, a two-stage crystallization sequence was performed using MELTS: equilibrium crystallization (EC) and fractional crystallization (FC). For details, see text.

composition and helps to keep olivine on the liquidus, giving shorter compositional gaps in olivine compared to the isobaric condition. The FC calculation starts at QFM−3.6, and decreases to QFM−4.0 to−4.3 in the temperature interval 1225 to 1115 °C in order to retain olivine as a phase in the fractionating assemblage, and to reconstruct the observed olivine and clinopyroxene zonation. At lower temperature, we used QFM−3.6, in order to reproduce the observed compositional range of plagioclase. In order to minimize the compositional gaps of olivine and increase the olivine stability as fractionation proceeds, we added 0.1 wt% H_2O to the starting liquid composition for the FC stage. A direct observational constraint on the H_2O content of the Tissint liquid is lacking, but totally anhydrous conditions are unlikely and small amounts of H_2O stored in nominally anhydrous minerals have been inferred from shock melts (Chen et al. 2015). Furthermore, we decreased the Cr_2O_3 content of the starting liquid for the FC stage (to 0.4 wt%) close to the value in one of the two analyses by Chennaoui Aoudjehane et al. (2012), in order to delay chromite crystallization until the olivine reaches a composition of Fo_{76} as observed.

This two-stage approach using MELTS produces a crystallization sequence broadly consistent with that observed in Tissint (Fig. 12). The predicted sequence from MELTS is: olivine → orthopyroxene → "spinel" → clinopyroxene-1 → clinopyroxene-2, 3 → whitlockite → plagioclase. It is important to note that whitlockite is used to represent all anhydrous phosphates in MELTS. In our calculations, phosphate appears at slightly higher temperature than plagioclase, which may reflect an imperfect combination of the conditions, but the general idea of phosphate saturation late in the sequence is reasonable.

The calculated mineral compositions of the FC stage reproduce several observations (Fig. 12). The early olivine is Fo_{80} continuing from the EC stage, and evolves toward more Fe-rich compositions. The predicted orthopyroxene composition at 1260–1285 °C matches the observed compositions (Fig. 12). Calculated clinopyroxene-1 with a composition of Wo_5En_{67} to $Wo_{17}En_{48}$ matches the results shown in Fig. 6. The predicted initial Ca-rich augite composition (either early clinopyroxene-2, $Wo_{33}En_{43}$, at 1132 °C and 8.2 MPa; or clinopyroxene-1, $Wo_{35}En_{41}$, at ~1124 °C and 7.3 MPa) is broadly similar to measured values. Compositional

variations for spinel-group minerals predicted from MELTS are consistent with the observed values. Predicted chromite saturation starts at 1289 °C with a composition of Cr# 79 and Ti# 3, similar to the observed chromite cores, and becomes progressively Ti-enriched, matching the observed spinel rim at 1054–1055 °C (9 mole% Cr# and 85 mole% Ti#). Furthermore, chromite appearance coincides with Fo_{76}, in accordance with observations. Plagioclase with a composition of An_{73} appears on the liquidus at 1115 °C; the measured composition of An_{67} appears at 1071 °C and becomes progressively more Na-rich. The composition of plagioclase varies with continued cooling and reaches An_{55} at 1019 °C, which matches the measured composition of plagioclase rims.

After a detailed, but not exhaustive search over crystallization conditions and starting compositions, some misfits between observation and prediction remain (Fig. 12). Some may reflect the limitations of the MELTS calibration and the mineral phases it considers; others may reflect unmodeled complexity in the evolution of the Tissint magma. The predicted olivine shows three compositional gaps, Fo_{67} to Fo_{62}, Fo_{61} to Fo_{49}, and then Fo_{49} to Fo_{47}. Then, olivine evolves from Fo_{49} to Fo_3 at 1019 °C, at which temperature the last liquid is consumed. The predicted compositional gaps and olivine with Fo < 35 are not observed in our samples. The simulation also predicts formation of multiple pyroxenes: orthopyroxene at 1325–1285 °C and a range of clinopyroxenes at $T < 1285$ °C. The Fe-rich augite compositions predicted for clinopyroxene-1 at $T < 1100$ °C are not observed. The cocrystallization of clinopyroxene-2 and low-T clinopyroxene-1 is likely an artifact of poorly resolved miscibility gaps toward high-Ti, Al compositions in the MELTS pyroxene model. The lack of Fe-rich olivine and Fe-rich clinopyroxene in the samples, predicted by MELTS at $<1100 \pm 20$ °C, could be explained if the system reverted to equilibrium crystallization during the waning stages, during which the mineral rims equilibrated with the residual melt until complete solidification.

The general agreement between the observed petrography and mineral chemistry of Tissint with the results of MELTS simulations confirms that the Tissint has a complex petrologic history. Although there are some discrepancies between observation and simulation, the Tissint petrogenesis can be broadly explained with a two-stage crystallization process, involving an early equilibrium stage followed by a polybaric fractional crystallization stage. Physically, two-stage crystallization is plausible, if the magma initially resided at a deeper crustal level and experienced slower cooling, and was then displaced to shallower depth where it cooled much faster. The displacement could be caused by any of the triggers commonly associated with destabilization of magma chambers and onset of magma ascent and possible eruption, e.g., recharge of the magma chamber. Alternatively, the transition from equilibrium to fractional crystallization could be a simple result of the geothermal gradient in the Martian crust. In this scenario, the rising magma is progressively in contact with cooler rocks, causing an increasing rate of heat loss from the magma to the surrounding rocks, and therefore an accelerating crystallization process.

Acknowledgments—We thank Allan Patchen and Luca Fedele for their assistance with data collection. Comments from the AE (C. Goodrich), T. Usui, C. Herd, and M. McCanta on earlier versions of the manuscript have significantly improved the presentation and are greatly appreciated. We acknowledge partial support by NASA Cosmochemistry grants NNX11AG58G to LAT, NNN13D465T to YL, NSF Grant EAR-1226270 to PDA, and NSF Grant EAR-1019770 to RJB. YL is supported by the Jet Propulsion Laboratory, which is managed by the California Institute of Technology under a contract with NASA.

Editorial Handling—Dr. Cyrena Goodrich

REFERENCES

Anders E. and Grevesse N. 1989. Abundances of the elements: Meteoritic and solar. *Geochimica et Cosmochimica Acta* 53:197–214.

Asimow P. D. 1999. A model that reconciles major- and trace-element data from abyssal peridotites. *Earth and Planetary Science Letters* 169:303–319.

Asimow P. D. and Ghiorso M. S. 1998. Algorithmic modifications extending MELTS to calculate subsolidus phase relations. *American Mineralogist* 83:1127–1131.

Asimow P. D., Hirschmann M. M., and Stolper E. M. 2001. Calculation of peridotite partial melting from thermodynamic models of minerals and melts. IV. Adiabatic decompression and the composition and mean properties of mid-ocean ridge basalts. *Journal of Petrology* 42:963–998.

Asimow P. D., Dixon J. E., and Langmuir C. H. 2004. A hydrous melting and fractionation model for mid-ocean ridge basalts: Application to the Mid-Atlantic Ridge near the Azores. *Geochemistry Geophysics Geosystems* 5: Q01E16.

Balta J. B. and McSween H. Y. 2013. Application of the MELTS algorithm to Martian compositions and implications for magma crystallization. *Journal of Geophysical Research: Planets* 118:2013JE004461.

Balta J. B., Sanborn M. E., Udry A., Wadhwa M., and McSween H. Y. 2015. Petrology and trace element geochemistry of Tissint, the newest shergottite fall. *Meteoritics & Planetary Science* 50:63–85.

Barrat J. A., Jambon A., Ferrière L., Bollinger C., Langlade J. A., Liorzou C., Boudouma O., and Fialin M. 2014. No

Martian soil component in shergottite meteorites. *Geochimica et Cosmochimica Acta* 125:23–33.

Basu Sarbadhikari A., Day J. M. D., Liu Y., Rumble D. III, and Taylor L. A. 2009. Petrogenesis of olivine-phyric shergottite Larkman Nunatak 06319: Implications for enriched components in Martian basalts. *Geochimica et Cosmochimica Acta* 73:2190–2214.

Basu Sarbadhikari A., Goodrich C. A., Liu Y., Day J. M. D., and Taylor L. A. 2011. Evidence for heterogeneous enriched shergottite mantle sources in Mars from olivine-hosted melt inclusions in Larkman Nunatak 06319. *Geochimica et Cosmochimica Acta* 75:6803–6820.

Baziotis I. P., Liu Y., DeCarli P. S., Melosh H. J., McSween H. Y., Bodnar R. J., and Taylor L. A. 2013. The Tissint Martian meteorite as evidence for the largest impact excavation. *Nature Communications* 4:1404.

Beattie P., Ford C., and Russell D. 1991. Partition coefficients for olivine-melt and orthopyroxene-melt systems. *Contributions to Mineralogy and Petrology* 109:212–224.

Bläß U. W., Langenhorst F., and McCammon C. 2010. Microstructural investigations on strongly stained olivines of the chassignite NWA 2737 and implications for its shock history. *Earth and Planetary Science Letters* 300:255–263.

Borg L. E. and Draper D. S. 2003. A petrogenetic model for the origin and compositional variation of the Martian basaltic meteorites. *Meteoritics & Planetary Science* 38:1713–1731.

Borg L. E., Nyquist L. E., Wiesmann H., and Reese Y. 2002. Constraints on the petrogenesis of Martian meteorites from the Rb-Sr and Sm-Nd isotopic systematics of the lherzolitic shergottites ALH 77005 and LEW 88516. *Geochimica et Cosmochimica Acta* 66:2037–2053.

Borg L. E., Nyquist L. E., Wiesmann H., Shih C. Y., and Reese Y. 2003. The age of Dar al Gani 476 and the differentiation history of the martian meteorites inferred from their radiogenic isotopic systematics. *Geochimica et Cosmochimica Acta* 67:3519–3536.

Brennecka G. A., Borg L. E., and Wadhwa M. 2014. Insights into the Martian mantle: The age and isotopics of the meteorite fall Tissint. *Meteoritics & Planetary Science* 49:412–418.

Castle N. and Herd C. D. K. 2014. Observational and experimental results for Tissint magma formation: The story thus far (abstract #2334). 45th Lunar and Planetary Science Conference. CD-ROM.

Chen Y., Liu Y., Guan Y., Eiler J. M., Ma C., Rossman G. R., and Taylor L. A. 2015. Evidence in Tissint for recent subsurface water on Mars. *Earth and Planetary Science Letters* 425:55–63.

Chennaoui Aoudjehane H., Avice G., Barrat J. A., Boudouma O., Chen G., Duke M. J. M., Franchi I. A., Gattacceca J., Grady M. M., Greenwood R. C., Herd C. D. K., Hewins R., Jambon A., Marty B., Rochette P., Smith C. L., Sautter V., Verchovsky A., Weber P., and Zanda B. 2012. Tissint Martian meteorite: A fresh look at the interior, surface, and atmosphere of Mars. *Science* 338:785–788.

Davidson J. P., Morgan D. J., Charlier B. L. A., Harlou R., and Hora J. M. 2007. Microsampling and iotopic analysis of igneous rocks: Implications for the study of magmatic systems. *Annual Review of Earth and Planetary Sciences* 35:273–311.

Dohmen R. and Chakraborty S. 2007. Fe–Mg diffusion in olivine II: Point defect chemistry, change of diffusion mechanisms and a model for calculation of diffusion coefficients in natural olivine. *Physics and Chemistry of Minerals* 34:409–430.

El Goresy A., Gillet P., Miyahara M., Ohtani E., Ozawa S., Lin Y., Feng L., and Escerig S. 2013. Multiple shock events and diamond formation on Mars (abstract #1037). 44th Lunar and Planetary Science Conference. CD-ROM.

Filiberto J. and Dasgupta R. 2011. Fe^{2+}–Mg partitioning between olivine and basaltic melts: Applications to genesis of olivine-phyric shergottites and conditions of melting in the Martian interior. *Earth and Planetary Science Letters* 304:527–537.

Filiberto J., Jackson C., Le L., and Treiman A. H. 2009. Partitioning of Ni between olivine and an iron-rich basalt: Experiments, partition models, and planetary implications. *American Mineralogist* 94:256–261.

Filiberto J., Musselwhite D. S., Gross J., Burgess K., Le L., and Treiman A. H. 2010. Experimental petrology, crystallization history, and parental magma characteristics of olivine-phyric shergottite NWA 1068: Implications for the petrogenesis of "enriched" olivine-phyric shergottites. *Meteoritics & Planetary Science* 45:1258–1270.

Ghiorso M. S. and Sack R. O. 1995. Chemical mass transfer in magmatic systems processes IV. A revised and internally consistent thermodynamic model for the interpolation and extrapolation of liquid-solid equilibria in magmatic systems at elevated temperatures and pressures. *Contributions to Mineralogy and Petrology* 119:197–212.

Ghiorso M. S., Hirschmann M. M., Reiners P. W., and Kress V. C. 2002. The pMELTS: A revision of MELTS for improved calculation of phase relations and major element partitioning related to partial melting of the mantle to 3 GPa. *Geochemistry, Geophysics, Geosystems* 3: 1–35. doi:10.1029/2001GC000217.

Goodrich C. A. 2003. Petrogenesis of olivine-phyric shergottites Sayh al Uhaymir 005 and Elephant Moraine A79001 lithology A. *Geochimica et Cosmochimica Acta* 67:3735–3772.

Gross J., Treiman A. H., Filiberto J., and Herd C. D. K. 2011. Primitive olivine-phyric shergottite NWA 5789: Petrography, mineral chemistry, and cooling history imply a magma similar to Yamato-980459. *Meteoritics & Planetary Science* 46:116–133.

Grosshans T., Lapen T., Andreasen R., and Irving A. 2013. Lu-Hf and Sm-Nd ages and source compositions for depleted shergottite Tissint (abstract #2872). 44th Lunar and Planetary Science Conference. CD-ROM.

Herd C. D. K., Dwarzski R. E., and Shearer C. K. 2009. The behavior of Co and Ni in olivine in planetary basalts: An experimental investigation. *American Mineralogist* 94:244–255.

Hu J., Sharp T. G., and Walton E. L. 2013. Shock effects in Tissint II: Olivine transformation to silicate perovskite and oxide (abstract #1041). 44th Lunar and Planetary Science Conference. CD-ROM.

Irving A. J., Kuehner S. M., Tanaka R., Herd C. D. K., Chen G., and Lapen T. J. 2012. The Tissint depleted permafic olivine-phyric shergottite: Petrologic, elemental and isotopic characterization of a recent martian fall in Morocco (abstract #2510). 43rd Lunar and Planetary Science Conference. CD-ROM.

Jerram D. A. and Martin V. M. 2008. Understanding crystal populations and their significance through the magma plumbing system. *Geological Society of London Special Publication* 304:133–148.

Jolliff B. L., Hughes J. M., Freeman J. J., and Zeigler R. A. 2006. Crystal chemistry of lunar merrillite and comparison to other meteoritic and planetary suites of whitlockite and merrillite. *American Mineralogist* 91:1583–1595.

Jurewicz A. G. and Watson E. B. 1988. Cations in olivine, Part 2: Diffusion in olivine xenocrysts, with applications to petrology and mineral physics. *Contributions to Mineralogy and Petrology* 99:186–201.

Kuchka C. R., Walton E. L., and Herd C. D. K. 2013. Shock melt features in Los Angeles and Tissint: A comparison (abstract #3043). 44th Lunar and Planetary Science Conference. CD-ROM.

Liu Y., Balta J. B., Goodrich C. A., McSween H. Y. Jr., and Taylor L. A. 2013. New constraints on the formation of shergottite Elephant Moraine 79001 lithology A. *Geochimica et Cosmochimica Acta* 108:1–20.

Longhi J. and Pan V. 1989. The parent magmas of the SNC meteorites. Proceedings, 19th Lunar and Planetary Science Conference. pp. 451–464.

Longhi J., Durand S. R., and Walker D. 2010. The pattern of Ni and Co abundances in lunar olivines. *Geochimica et Cosmochimica Acta* 74:784–798.

Ma C., Tschauner O, Liu Y., Beckett J. R., Rossman G. R., Zuravlev K., Prakapenka V., Dera P., Sinogeikin S., and Taylor L. A. 2014. Discovery of Ahrensite γ- Fe_2SiO_4 and Tissintite (Ca, Na,γ)$AlSi_2O_6$: Two new high-pressure minerals from the Tissint Martian meteorite (abstract #1222). 45th Lunar and Planetary Science Conference. CD-ROM.

Ma C., Tschauner O., Beckett J. R., Liu Y., Rossman G. R., Zhuravlev K., Prakapenka V., Dera P., and Taylor L. A. 2015. Tissintite, (Ca, Na, γ)$AlSi_2O_6$, a highly-defective, shock-induced, high-pressure clinopyroxene in the Tissint Martian meteorite. *Earth and Planetary Science Letters* 422:194–205.

Ma C., Tschauner O., Beckett J. R., Liu Y., Rossman G. R., Sinogeikin S. V., Smith J. S., and Taylor L. A. 2016. Ahrensite, γ-Fe_2SiO_4, a new shock-metamorphic mineral from the Tissint meteorite: Implications for the Tissint shock event on Mars. *Geochimica et Cosmochimica Acta* 184:240–256.

McSween H. Y. Jr. and Jarosewich E. 1983. Petrogenesis of the Elephant Moraine A79001 meteorite: Multiple magma pulses on the shergottite parent body. *Geochimica et Cosmochimica Acta* 47:1501–1513.

Mikouchi T., Miyamoto M., and McKay G. A. 2001. Mineralogy and petrology of the Dar al Gani 476 Martian meteorite: Implications for its cooling history and relationship to other shergottites. *Meteoritics & Planetary Science* 36:531–548.

Milman-Barris M., Beckett J., Baker M., Hofmann A., Morgan Z., Crowley M., Vielzeuf D., and Stolper E. 2008. Zoning of phosphorus in igneous olivine. *Contributions to Mineralogy and Petrology* 155:739–765.

Mutchler S. R., Fedele L., and Bodnar R. J. 2008. Analysis Management System (AMS) for reduction of laser ablation ICPMS data. In *Laser-Ablation-ICPMS in the Earth sciences: Current practices and outstanding issues*, edited by Sylvester P. *Mineralogical Association of Canada Short Course Series* 40:318–327.

Papike J. J., Karner J. M., Shearer C. K., and Burger P. V. 2009. Silicate mineralogy of Martian meteorites. *Geochimica et Cosmochimica Acta* 73:7443–7485.

Park J., Herzog G. F., Nyquist L. E., Shih C.-Y., Turrin B., Lindsay F. N., Delaney J. S., Swisher C. C. III, and Agee C. 2013. Ar-Ar and Rb-Sr ages of the Tissint olivine-phyric Martian shergottite (abstract #5320). 76th Annual Meeting of the Meteoritical Society. Meteoritics & Planetary Science 48.5320.pdf.

Pernet-Fisher J. F., Howarth G. H., Liu Y., Barry P. H., Carmody L., Valley J. W., Bodnar R. J., Spetsius Z. V., and Taylor L. A. 2014. Komsomolskaya diamondiferous eclogites: Evidence for oceanic crustal protoliths. *Contributions to Mineralogy and Petrology* 167:1–17.

Peslier A. H., Hnatyshin D., Herd C. D. K., Walton E. L., Brandon A. D., Lapen T. J., and Shafer J. T. 2010. Crystallization, melt inclusion, and redox history of a Martian meteorite: Olivine-phyric shergottite Larkman Nunatak 06319. *Geochimica Et Cosmochimica Acta* 74:4543–4576.

Peters T. J., Simon J. I., Jones J. H., Usui T., Moriwaki R., Economos R. C., Schmitt A. K., and McKeegan K. D. 2015. Tracking the source of the enriched martian meteorites in olivine-hosted melt inclusions of two depleted shergottites, Yamato 980459 and Tissint. *Earth and Planetary Science Letters* 418:91–102.

Pieters C. M., Klima R. L., Hiroi T., Dyar M. D., Lane M. D., Treiman A. H., Noble S. K., Sunshine J. M., and Bishop J. L. 2008. Martian dunite NWA 2737: Integrated spectroscopic analyses of brown olivine. *Journal of Geophysical Research: Planets* 113:E06004.

Shearer C. K., Burger P. V., Papike J. J., Borg L. E., Irving A. J., and Herd C. D. K. 2008. Petrogenetic linkages among Martian basalts: Implications based on trace element chemistry of olivine. *Meteoritics & Planetary Science* 43:1241–1258.

Shearer C. K., Papike J. J., Burger P. V., Sutton S. R., McCubbin F. M., and Newville M. 2011. Direct determination of europium valence state by XANES in extraterrestrial merrillite: Implications for REE crystal chemistry and Martian magmatism. *American Mineralogist* 96:1418–1421.

Shearer C. K., Aaron P. M., Burger P. V., Guan Y., Bell A. S., and Papike J. J. 2013. Petrogenetic linkages among fO2, isotopic enrichments-depletions and crystallization history in Martian basalts. Evidence from the distribution of phosphorus in olivine megacrysts. *Geochimica et Cosmochimica Acta* 120:17–38.

Shearer C. K., Burger P. V., Papike J. J., McCubbin F. M., and Bell A. S. 2015. Crystal chemistry of merrillite from Martian meteorites: Mineralogical recorders of magmatic processes and planetary differentiation. *Meteoritics & Planetary Science* 50:649–673.

Shih C.-Y., Nyquist L. E., Park J., and Agee C. B. 2014. Sm-Nd and Rb-Sr isotopic systematics of a heavily shocked Martian meteorite Tissint and petrogenesis of depleted shergottites (abstract #1184). 45th Lunar and Planetary Science Conference. CD-ROM.

Smith P. M. and Asimow P. D. 2005. Adiabat_1ph: A new public front-end to the MELTS, pMELTS, and pHMELTS models. *Geochemistry, Geophysics, Geosystems* 6:Q02004.

Sonzogni Y. and Treiman A. H. 2013. Small melt inclusions in olivines from Martian meteorites: Value for constraining original melt compositions (abstract #1049). 44th Lunar and Planetary Science Conference. CD-ROM.

Summerson I., Greshake A., Fritz J., and Reimold W. U. 2013. High-pressure phases in a melt pocket within an olivine macrocryst in the Tissint Martian meteorite (abstract #1974). 44th Lunar and Planetary Science Conference. CD-ROM.

Symes S. J. K., Borg L. E., Shearer C. K. and Irving A. J. 2008. The age of the Martian meteorite Northwest Africa 1195 and the differentiation history of the shergottites. *Geochimica et Cosmochimica Acta* 72:1696–1710.

Taylor L. A., Onorato P. I. K., and Uhlmann D. R. 1977. Cooling rate estimations based on kinetic modelling of Fe-Mg diffusion in olivine. Proceedings, 8th Lunar Science Conference. pp. 1581–1592.

Treiman A. H., Dyar M. D., McCanta M., Noble S. K., and Pieters C. M. 2007. Martian Dunite NWA 2737: Petrographic constraints on geological history, shock events, and olivine color. *Journal of Geophysical Research* 112:E04002.

Tschauner O., Asimow P. D., Kostandova N., Ahrens T. J., Ma C., Sinogeikin S., Liu Z., Fakra S., and Tamura N. 2009. Ultrafast growth of wadsleyite in shock-produced melts and its implications for early solar system impact processes. *Proceedings of the National Academy of Sciences* 106:13,691–13,695.

Udry A., McSween H. Y. Jr., Lecumberri-Sanchez P., and Bodnar R. J. 2012. Paired nakhlites MIL 090030, 090032, 090136, and 03346: Insights into the Miller Range parent meteorite. *Meteoritics & Planetary Science* 47:1575–1589.

Usui T., McSween H. Y., and Floss C. 2008. Petrogenesis of olivine-phyric shergottite Yamato 980459, revisited. *Geochimica Et Cosmochimica Acta* 72:1711–1730.

Vinet N. and Higgins M. D. 2010. Magma solidification processes beneath Kilauea volcano, Hawaii: A quantitative textural and geochemical study of the 1969–1974 Mauna Ulu lavas. *Journal of Petrology* 51:1297–1332.

Walton E. L., Sharp T. G., Hu J., and Filiberto J. 2014. Heterogeneous mineral assemblages in Martian meteorite Tissint as a result of a recent small impact event on Mars. *Geochimica et Cosmochimica Acta* 140:334–348.

SUPPORTING INFORMATION

Additional supporting information may be found in the online version of this article:

Fig. S1. Abundances of trace elements in the Tissint minerals normalized using those in CI-chondrite of Anders and Grevesse (1989). (a) REE. (b) Extended trace element plot, showing that Sr and Ti in merrillite are strongly depleted, Ti depletion in maskelynite is weaker, whereas Ti in pyroxenes show positive anomaly.

Fig. S2. Composition of chromite and ulvöspinel in Tissint. The inset plots the mole% of chromite with Mg# in the Fe-Ti spinel. The chromite shows progressive depletion in Mg# with crystallization, followed by enrichment in Ti, as the spinel continues crystallization towards the ulvöspinel end-member.

Fig. S3. Extended trace-element plot of the Tissint impact melt (imp gl) and fusion crust, in comparison with literature data of Tissint and those of three chemical groups of shergottites. Chondrite values used for normalization are from Anders and Grevesse (1989). The fields for three chemical groups are from Basu Sarbadhikari et al. (2009). For clarity, QUE 94201 in the depleted group is not plotted.

Table S1. LA-ICP-MS data of selected minerals and glass. EMP data are included for comparison.